

## Computer simulations of rapid granular flows of spheres interacting with a flat, frictional boundary

Cite as: Physics of Fluids **6**, 2253 (1994); <https://doi.org/10.1063/1.868178>

Submitted: 09 June 1993 • Accepted: 23 March 1994 • Published Online: 02 September 1998

Michel Y. Louge



View Online



Export Citation

### ARTICLES YOU MAY BE INTERESTED IN

[On dense granular flows down flat frictional inclines](#)

Physics of Fluids **13**, 1213 (2001); <https://doi.org/10.1063/1.1358870>

[On the flux of fluctuation energy in a collisional grain flow at a flat, frictional wall](#)

Physics of Fluids **9**, 2835 (1997); <https://doi.org/10.1063/1.869396>

[Measurements of the collision properties of small spheres](#)

Physics of Fluids **6**, 1108 (1994); <https://doi.org/10.1063/1.868282>



**APL Machine Learning**

**Open, quality research for the networking communities**

MEET OUR NEW **EDITOR-IN-CHIEF**

[LEARN MORE](#)

# Computer simulations of rapid granular flows of spheres interacting with a flat, frictional boundary

Michel Y. Louge

*Sibley School of Mechanical and Aerospace Engineering, Cornell University, Ithaca, New York 14853*

(Received 9 June 1993; accepted 23 March 1994)

This paper employs computer simulations to test the theory of Jenkins [J. Applied Mech. **59**, 120 (1992)] for the interaction between a rapid granular flow of spheres and a flat, frictional wall. This paper examines the boundary conditions that relate the shear stress and energy flux at the wall to the normal stress, slip velocity, and fluctuation energy, and to the parameters that characterize a collision. It is found that while the theory captures the trends of the boundary conditions at low friction, it does not anticipate their behavior at large friction. A critical evaluation of Jenkins' assumptions suggests where his theory may be improved.

## I. INTRODUCTION

A granular material is an aggregate of discrete solid particles. Rapid flows of granular materials occur in phenomena such as rock slides, debris flows, snow avalanches, planetary rings, and the motion of the Arctic ice pack and in industrial processes involving the bulk transport of coal, grain, and powders. In rapid granular flows, the interactions among the solid particles and those between the wall and the particles consist of a succession of instantaneous collisions. These collisions create random fluctuations of the grain velocities, which are responsible for the transport of momentum and fluctuation energy through the flow.

Because in these flows typical length scales are of order the particle diameter, boundaries play a pervasive role there. An indication of the role of the boundaries is provided by the experiments on the rapid shearing of glass spheres performed by Savage and Sayed<sup>1</sup> and Hanes and Inman.<sup>2</sup> In order to transfer momentum and energy to the flow, Savage and Sayed covered their boundaries with sandpaper, while Hanes and Inman cemented glass spheres to theirs. At the same shear rate and density, Hanes and Inman measured shear stresses approximately three times higher than those of Savage and Sayed. In similar experiments with metals powders, Craig, Buckholz, and Domoto<sup>3</sup> observed considerably higher stresses with rough boundaries than smooth ones.

An insight into these phenomena is provided by the computer simulations performed, for example, by Campbell and Gong,<sup>4</sup> and Louge, Jenkins, and Hopkins<sup>5</sup> on two-dimensional rapid flows of disks, and by Kim and Rosato<sup>6</sup> on the similar flows of spheres. These simulations show how profiles of density, velocity, and fluctuation energy vary across the gap of a shear cell as the size, spacing, and collision properties of smooth particles attached to the boundaries are changed. The role of boundaries is further elucidated by the theories of Jenkins and Richman,<sup>7</sup> Jenkins,<sup>8</sup> Richman,<sup>9</sup> Hanes, Jenkins, and Richman,<sup>10</sup> Pasquarell and Ackermann,<sup>11</sup> and Pasquarell,<sup>12</sup> who calculate averages of the momentum and energy transferred in collisions between flow particles and a bumpy, frictionless wall.

The discrepancies observed among different experiments with inclined planes also suggest that the boundaries play a crucial role in rapid granular flows interacting with flat, frictional walls.

For example, the velocity profiles recorded in chute flows by Augenstein and Hogg<sup>13</sup> and Drake and Shreve<sup>14</sup> differ from those of Ishida and Shirai<sup>15</sup> and Savage.<sup>16</sup>

Generally, experimental progress has followed the introduction of new detailed measurement techniques. Recently, Ahn, Brennen, and Sabersky<sup>17</sup> cross-correlated the signals from two optical fiber bundles and inferred the mean particle velocity and one component of the velocity fluctuations in a inclined chute flow. In spite of such achievements, because of the considerable difficulties in performing and interpreting point measurements, experiments have seldom produced information precise enough to test the assumptions of the theory. Instead, the required details are obtained using computer simulations.

Several authors have simulated the interaction of granular flows with flat, frictional walls. For example, in two-dimensional flows of disks, Campbell and Brennen reported profiles of velocity, concentration and granular fluctuation energy,<sup>18,19</sup> and Zhang and Campbell<sup>20</sup> studied the interface between fluid-like and solid-like behavior. Nakagawa and Imaizumi<sup>21</sup> focused on mixtures consisting of spheres of two sizes flowing in a periodic Couette cell. Walton<sup>22</sup> investigated steady flows of frictional spheres down inclines. Unfortunately, because until recently theories for the interaction between rapid granular flows and a boundary were limited to bumpy, frictionless walls, those simulations were performed without a theory guiding the interpretation of their results.

Unlike flows of continuous fluids, rapid granular flows generally experience a significant relative average velocity between the flow particles and a flat boundary. Because of this, the wall may supply fluctuation energy to the flow from the working of its shear stress through the mean wall-particle slip. Consequently, boundary conditions for flat, frictional walls must be calculated, rather than assumed. To derive such conditions for models of granular flows and suspensions, Johnson and Jackson<sup>23</sup> employed heuristic arguments. They assumed that some of the particles were sliding relative to the boundary, and that their tangential and normal stresses were related by a Coulomb yield condition.

Recently, Jenkins<sup>24</sup> developed the first theory for rapid granular flows interacting with a flat, frictional wall. To this end, he focused his attention on collisions and incorporated

Coulomb friction into the collisional interactions with the wall. He employed a simple velocity distribution function to integrate the collisional impulse and change in fluctuation energy over all possible collisions in, and near, two limits. In the first limit, the coefficient of friction is so large that the particles do not slide upon contact with the wall. In the second, the coefficient is so small that all collisions involve sliding. In that work, Jenkins derived expressions for the ratio of shear to normal stresses and for the flux of fluctuation energy through the wall.

In the present paper our objective is to test Jenkins' theory through computer simulations. In particular, we examine the assumptions that Jenkins employed to render his calculations tractable, and we explore a wide range of collision properties for the wall and the flow particles. We begin with a description of the particle simulation. We then explore two regimes of flow that correspond to low and high values of the coefficient of friction.

## II. THE PARTICLE SIMULATION

We consider flows of identical, homogeneous, inelastic, frictional spheres in a periodic Couette geometry bounded by a flat, frictional wall and a two-dimensional, smooth array of half-spheres colliding and moving on a plane parallel to the flat wall.

### A. Collision search algorithm

The numerical simulations are carried out using an algorithm described by Hopkins and Louge.<sup>25</sup> After a given time step, the algorithm calculates the position of each particle from the previous position and velocity at the beginning of the interval. In simulations that involve gravity, a ballistic trajectory produces the appropriate changes in position and velocity during the time interval.

Collisions occur when a particle overlaps slightly with a neighbor or with the wall. After each particle has experienced an average of ten collisions, the algorithm calculates the mean overlap encountered in those collisions. The simulation time step is then readjusted so that the mean overlap does not exceed a given tolerance expressed as a fraction of the particle diameter. In order to establish the optimum tolerance for given flow conditions, simulations are run with decreasing values of the tolerance until all results of interest become insensitive to further reductions. These results include stresses and energy fluxes, as well as all measures of volume fraction and first and second moments of linear and angular velocities at the wall. In the present simulations with average particle volume fraction of 30%, the tolerance is generally set at a conservative 1% of the particle diameter. However, flows that exhibit a dense layer of particles near the flat wall are simulated with a tolerance of 0.5%. A search grid is superimposed on the flow domain to permit fast identification of near neighbors. The combination of this search grid and the hard particle/overlap technique described above permits the execution of these simulations on a computer of relatively modest size.<sup>25</sup>

## B. Collisions

The velocities of the particles emerging from a collision are calculated by considering the balance of linear and angular momenta in the collision. For consistency with Jenkins,<sup>24</sup> we employ Walton's simpler interpretation of the model of Maw, Barber, and Fawcett<sup>26,27</sup> to describe the dynamics of individual collisions.<sup>28</sup> During a collision, energy is stored in elastic deformations associated with both the normal and tangential displacements of the contact point relative to the center of the sphere. Because the release of this energy may affect the rebound significantly, we introduce coefficients of restitution associated with both the normal and tangential components of the velocity of the point of contact. Recent experiments with glass and acetate spheres in our laboratory have shown that this model is appropriate for both particle-particle and particle-wall collisions.<sup>29</sup>

We consider two colliding spheres of diameters  $\sigma_1$  and  $\sigma_2$  and masses  $m_1$  and  $m_2$  with centers located at  $\mathbf{r}_1$  and  $\mathbf{r}_2$ . We define the unit normal along the line joining the centers of the two spheres  $\mathbf{n} \equiv (\mathbf{r}_1 - \mathbf{r}_2)/|\mathbf{r}_1 - \mathbf{r}_2|$ . During the collision, sphere 2 exerts an impulse  $\mathbf{J}$  onto sphere 1. Prior to the collision, the spheres have translational velocities  $\mathbf{c}_1$  and  $\mathbf{c}_2$  and angular velocities  $\boldsymbol{\omega}_1$  and  $\boldsymbol{\omega}_2$ ; the corresponding post-collision velocities are denoted by primes. The velocities before and after the collision are related by

$$m_1(\mathbf{c}'_1 - \mathbf{c}_1) = -m_2(\mathbf{c}'_2 - \mathbf{c}_2) = \mathbf{J} \quad (1)$$

and

$$(2I_1/\sigma_1)(\boldsymbol{\omega}'_1 - \boldsymbol{\omega}_1) = (2I_2/\sigma_2)(\boldsymbol{\omega}'_2 - \boldsymbol{\omega}_2) = -\mathbf{n} \times \mathbf{J}, \quad (2)$$

where  $I = m\sigma^2/10$  is the moment of inertia about the center of a homogeneous sphere. In order to determine the impulse  $\mathbf{J}$ , we define the relative velocity  $\mathbf{g}$  of the point of contact,

$$\mathbf{g} = (\mathbf{c}_1 - \mathbf{c}_2) - \left( \frac{\sigma_1}{2} \boldsymbol{\omega}_1 + \frac{\sigma_2}{2} \boldsymbol{\omega}_2 \right) \times \mathbf{n}. \quad (3)$$

Using Eqs. (1) and (2), the contact velocities before and after the collision are related by

$$\mathbf{g}' - \mathbf{g} = (7/2m^*)\mathbf{J} - (5/2m^*)\mathbf{n}(\mathbf{J} \cdot \mathbf{n}), \quad (4)$$

where  $m^* \equiv (m_1^{-1} + m_2^{-1})^{-1}$  is the reduced mass. The usual coefficient of restitution  $e$  characterizes the incomplete restitution of the normal component of  $\mathbf{g}$ ,

$$\mathbf{n} \cdot \mathbf{g}' = -e\mathbf{n} \cdot \mathbf{g}, \quad (5)$$

where  $0 \leq e \leq 1$ .

In collisions that involve sliding, the sliding is assumed to be resisted by Coulomb friction and the tangential and normal components of the impulse are related by the coefficient of friction  $\mu$ ,

$$|\mathbf{n} \times \mathbf{J}| = \mu(\mathbf{n} \cdot \mathbf{J}), \quad (6)$$

where  $\mu \geq 0$ . Combining Eqs. (4)–(6) provides an expression for the impulse in terms of the normal and tangential components of  $\mathbf{g}$ ,

$$\begin{aligned} \mathbf{J}^{(1)} = & -m^*(1+e)(\mathbf{g} \cdot \mathbf{n})\mathbf{n} \\ & + \mu m^*(1+e) \cot \gamma [\mathbf{g} - \mathbf{n}(\mathbf{g} \cdot \mathbf{n})], \end{aligned} \quad (7)$$

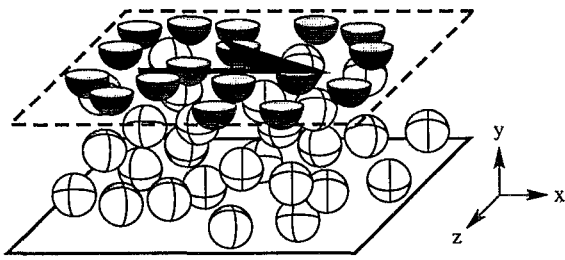


FIG. 1. Sketch of the Couette cell arrangement. Dimensions are not to scale. The shaded hemispheres of the top wall thermostat move at the average velocity  $U$  shown by the arrow. Only the central periodic domain is shown.

where the superscript (1) denotes collisions that involve sliding, and  $\gamma$  is the angle between  $\mathbf{g}$  and  $\mathbf{n}$ ,

$$\cot \gamma \equiv \mathbf{g} \cdot \mathbf{n} / |\mathbf{g} \times \mathbf{n}|. \quad (8)$$

As  $\gamma$  increases, sliding stops when

$$\mathbf{n} \times \mathbf{g}' = -\beta_0 \mathbf{n} \times \mathbf{g}, \quad (9)$$

or equivalently at a value  $\gamma_0$  of the collision angle such that

$$(1 + \beta_0) = -(7/2)(1 + e)\mu \cot \gamma_0, \quad (10)$$

where  $0 \leq \beta_0 \leq 1$  is the tangential coefficient of restitution. Collisions with  $\gamma \geq \gamma_0$  do not involve sliding, and in this case the impulse is found by combining Eqs. (4), (5), and (9),

$$\begin{aligned} \mathbf{J}^{(2)} = & -m^*(1 + e)(\mathbf{g} \cdot \mathbf{n})\mathbf{n} \\ & - (2m^*/7)(1 + \beta_0)[\mathbf{g} - \mathbf{n}(\mathbf{g} \cdot \mathbf{n})]. \end{aligned} \quad (11)$$

In this expression, the superscript (2) denotes collisions that do not involve sliding. Note that in this three-parameter formulation of the impact model,  $e$ ,  $\mu$ , and  $\beta_0$  are all constant.<sup>29</sup>

Collisions with the flat wall can be treated by considering the wall as a particle with infinite mass, so  $m^* = m$ . For collisions between two identical particles,  $m^* = m/2$ . In the present simulations, all interior particles are identical spheres of diameter  $\sigma$ , and collision properties  $e^p$ ,  $\mu^p$ , and  $\beta_0^p$ . In its collisions with interior particles, the flat, frictional wall has properties  $e$ ,  $\mu$ , and  $\beta_0$ .

### C. Periodic Couette flow domain

The flow domain is bounded by two parallel, flat, frictional walls located a distance  $L_y$  apart (Fig. 1). The bottom wall is fixed and the top wall moves at the velocity  $U$ . An orthogonal, Cartesian coordinate system attached to the bottom wall has direction  $\mathbf{x}$  along  $U$ , direction  $\mathbf{y}$  normal to the walls, and direction  $\mathbf{z}$ . An array of hemispheres of diameter  $\sigma$  is constrained to slide without dissipation or spin on the top wall with average velocity equal to  $U$ . These hemispheres are massive enough to be unaffected by collisions with interior particles but, through these collisions, they transfer momentum and fluctuation energy to the interior with collision properties  $e^p$ ,  $\mu^p$ , and  $\beta_0^p$ . In contrast, because the collisional interaction among these hemispheres is assumed to be frictionless with unit coefficient of normal restitution and zero tangential restitution, their two-dimensional granular temperature  $T_0$  is conserved, so they behave like an adjustable thermostat designed to energize the spheres in the interior.

The fraction of the surface area occupied by these hemispheres sliding on the top wall is  $\bar{v}_0$ . The interior particles occupy the fraction  $\bar{v}$  of the total volume of the flow domain.

The semi-infinite Couette geometry is approximated by a central periodic domain bounded by the two walls and consisting of an orthogonal parallelepiped of length  $L_x$ , width  $L_y$ , and depth  $L_z$  along the directions  $\mathbf{x}$ ,  $\mathbf{y}$ , and  $\mathbf{z}$ , respectively. The open boundaries of the domain are connected such that a sphere leaving the domain through one boundary simultaneously reenters the domain at the same relative location through the opposite boundary with the same velocity.

The conditions of a steady simulation are determined by 12 dimensionless parameters namely,  $U/\sqrt{T_0}$ ,  $e$ ,  $\mu$ ,  $\beta_0$ ,  $e^p$ ,  $\mu^p$ ,  $\beta_0^p$ ,  $\bar{v}_0$ ,  $\bar{v}$ ,  $L_y/\sigma$ , and the aspect ratios  $L_y/L_x$  and  $L_z/L_x$ . We adopt in the present simulations  $\bar{v}_0 = 57\%$ . Unless otherwise noted, the collision properties of interior particles are identical to those of the wall,  $\bar{v} = 30\%$  and  $L_z/L_x = 1$ .

### D. Steady state

Before running a series of simulations at given values of the collision properties, the interior particles are arranged in an expanded hexagonal array with average volume fraction  $\bar{v}$  and streamwise velocities equal to the product of the distance from the bottom wall and the average shear rate between the walls. Small random velocity fluctuations are added to initiate collisions. From this initial configuration, a simulation is carried out until each interior particle has collided on average 80 times with the bottom wall. This first run is designed to achieve a steady-state independent of the initial configuration of the system, as well as a two-dimensional Maxwellian velocity distribution among the hemispheres of the top wall thermostat.

For each new set of collision properties, a series of simulations is carried out at increasing or decreasing values of  $U/\sqrt{T_0}$ . The final configuration of a run (particle positions and velocities) is used as input to the next. For each new value of  $U/\sqrt{T_0}$ , a steady state is first achieved by running a simulation long enough for each particle to collide on average 40 times with the bottom wall. Then, statistics of the flow parameters are computed during another run of similar duration.

### E. Statistics

In his recent paper, Jenkins<sup>24</sup> calculated the impulse and change in kinetic energy in a typical collision with the flat, frictional wall and, using a simple velocity distribution function, obtained the rates at which momenta and energy are supplied to the flow over a unit area of the wall. From these, he determined boundary conditions that relate the shear stress and energy flux in the flow at the wall to the normal stress, slip velocity, and fluctuation energy, and to the parameters  $e$ ,  $\mu$ , and  $\beta_0$  that characterize the collision with the wall.

The boundary conditions are given in terms of the mean velocity  $\mathbf{g}_0$  of the contact point relative to the boundary. This slip velocity is defined in terms of the average velocity  $\langle \langle \mathbf{c} \rangle \rangle_0$

of the flow at the wall, the mean angular velocity  $\langle\langle\omega\rangle\rangle_0$  of the particles there, and the unit vector  $\mathbf{n}$  normal to the wall by

$$\mathbf{g}_0 = \langle\langle\mathbf{c}\rangle\rangle_0 + (\sigma/2)\mathbf{n} \times \langle\langle\omega\rangle\rangle_0. \quad (12)$$

In Jenkins' formulation, the average of a property  $\psi$  that is a function of  $\mathbf{c}$  and  $\omega$  is defined by

$$\langle\langle\psi\rangle\rangle = \frac{1}{n^*} \int \int \psi(\mathbf{c}, \omega) f(\mathbf{c}, \omega) d\mathbf{c} d\omega, \quad (13)$$

where the integration is over all  $\mathbf{c}$  and  $\omega$ , and  $f$  is a velocity distribution function normalized so its integral over all  $\mathbf{c}$  and  $\omega$  is equal to the particle number density  $n^*$ . Jenkins normalizes the magnitude of the slip velocity using the translational granular temperature  $T$  of the flow at the wall and thus defines

$$r = g_0 / \sqrt{3T}, \quad (14)$$

where  $T = (1/3)\langle\langle C^2 \rangle\rangle$  and  $\mathbf{C} = \mathbf{c} - \langle\langle\mathbf{c}\rangle\rangle$ . By changing the ratio  $U/\sqrt{T_0}$ , the present simulations can produce a wide range of steady values of  $r$  at the bottom wall. Without this capability, they would only yield one  $r$  for a given set of collision properties. Jenkins also introduces the spin fluctuation velocity  $\Omega = (\sigma/\sqrt{10})(\omega - \langle\langle\omega\rangle\rangle)$  and the corresponding rotational granular temperature  $\tau = (1/3)\langle\langle\Omega^2\rangle\rangle$ .

Jenkins calculates the collisional rate of change  $C(\psi)$  of  $\psi$  per unit area of the wall as the integral of the change in  $\psi$  in a single collision over the rate of collisions per unit area,

$$C(\psi) = -\chi \int \int (\psi' - \psi) f(\mathbf{c}, \omega) \mathbf{c} \cdot \mathbf{n} d\mathbf{c} d\omega, \quad (15)$$

where the integration is taken over all  $\omega$  and over all values of  $\mathbf{c}$  for which impending collisions are possible,  $\mathbf{c} \cdot \mathbf{n} \leq 0$ . Jenkins introduces the factor  $\chi$  to take into account the presence of the wall on the spatial distribution of the particles. Thus  $\chi$  is the value of the spatial distribution function  $g_{12}$  for spheres touching the wall. For flows with constant volume fraction  $\nu^*$  in the bulk, the product  $\chi\nu^*$  is the local value of the volume fraction at the wall.

From (15) Jenkins calculates the boundary traction  $\mathbf{M}$  as the mean collisional rate of change of the particle momentum per unit area of the wall,

$$\mathbf{M} = C(m\mathbf{c}). \quad (16)$$

Its components are the shear stress ( $-S$ ) and normal stress  $N$  applied by the wall to the flow.

Jenkins considers the energy balance across an infinitesimal volume adjacent to the wall, and writes the magnitude  $Q$  of the flux of fluctuation energy supplied by the wall to the flow in terms of  $\mathbf{M}$  and  $\mathbf{g}_0$  as

$$Q = -\mathbf{g}_0 \cdot \mathbf{M} - D. \quad (17)$$

Here  $D$  is the rate of dissipation of the energy of the particles per unit area of the wall,

$$-D = C(mc^2/2 + I\omega^2/2). \quad (18)$$

Fluctuation energy is provided to the flow when the working of the boundary traction  $\mathbf{M}$  through its velocity  $-\mathbf{g}_0$  exceeds the dissipation  $D$ .

In the present simulations,  $\mathbf{M}$  is calculated by averaging the normal and tangential components of the momentum imparted to the colliding spheres by the boundary per unit wall area and unit time. The dissipation  $D$  is found by averaging in a similar way the change of translational and rotational kinetic energies of each particle involved in a collision with the bottom wall. Transverse profiles of the average particle volume fraction and the first and second moments of the linear and angular velocities are calculated by dividing the flow domain into a number  $i$  of horizontal strips of width  $L_y/i$ , length  $L_x$ , and depth  $L_z$ . The contributions of these quantities to each strip are averaged over a number of successive flow realizations separated by the time necessary to have one third of all flow particles collide once on average with the bottom wall.

We distinguish two possible means of averaging a flow parameter  $\psi$  in the strips. The first is the "mass average." We denote it with the symbol  $\langle\psi\rangle$ . Here, a sphere with property  $\psi$  contributes to a strip if any part of the sphere intersects the strip. The contribution of the sphere to  $\psi$  is weighed according to the mass of the sphere that intersects the strip. In particular, the mass-averaged volume fraction  $\langle\nu\rangle$  in a strip is the total solid mass in the strip divided by the volume of the strip and the material density of the spheres.

The second is the "center average" denoted by the symbol  $\leq\psi\geq$ . In this case, a sphere contributes its entire magnitude of  $\psi$  to the strip where its center is located. This latter form of averaging is inherently more noisy than the former. However, it provides values of the local volume fraction  $\leq\nu\geq$  that are consistent with the formalism of the collision integral (15), which incorporates the probability of sphere centers to lie within an infinitesimal volume near the point of impact. Because spheres cannot penetrate the wall, the first nonzero center-average value of  $\leq\nu\geq$  is located at  $y/\sigma = 1/2$ . Because the spheres touching the wall contribute their entire mass to the first strip, the magnitude  $\leq\nu\geq_{\sigma/2}$  of the local volume fraction there may exceed one.

In most simulations, the strip width is approximately 12% of the sphere diameter. In simulations that require the precise determination of  $\langle\nu\rangle$  and  $\leq\nu\geq$  at a distance  $y = \sigma/2$  from the wall, the strip width is 1.7% of  $\sigma$ . Because in typical simulations the first and second moments of the linear and angular velocities vary slowly near the wall, and because the mass-average values of these at  $y=0$  is nearly equal to the corresponding center averages at  $y/\sigma = 1/2$ , the appropriate mass averages from the strip closest to the wall yield accurate estimates of  $T$ ,  $\tau$ , and  $\mathbf{g}_0$  there. Finally, the flux  $Q$  is calculated through (17) using the values of  $\mathbf{M}$ ,  $\mathbf{g}_0$ , and  $D$  produced by the simulation.

### III. RESULTS

We distinguish two regimes of flow. The first appears when the coefficient of friction  $\mu$  is moderate. Typically, this corresponds to  $\mu \leq 0.4$ . There, the spheres may or may not slide upon contact with the flat wall. In contrast, for values of  $\mu$  larger than about 1.5, the spheres seldom slide upon contact, so they experience an impulse nearly always equal to  $\mathbf{J}^{(2)}$ . In this regime, the stresses and the flux of fluctuation energy through the wall become independent of  $\mu$ .

In this section we compare the simulation results with the predictions of Jenkins' theory in the low and high friction regimes.

### A. Jenkins' theory

Jenkins calculates the shear and normal stresses and the flux of fluctuation energy through the wall in two asymptotic limits. To avoid complicated integrations, he restricts his attention to  $r \geq 1$ . Because the distinction between sliding and nonsliding collisions is central to the analysis, see Eq. (10), the coefficient of friction often enters Jenkins' calculations through the parameter  $\bar{\mu}_0$  given by

$$\bar{\mu}_0 = -\tan \gamma_0 = (7/2)\mu(1+e)/(1+\beta_0). \quad (19)$$

In the first limit, the coefficient of friction is large,  $\mu > \mu/\bar{\mu}_0$  and particles do not slide. This is the "large friction/no sliding" limit. In this case, the "dynamic friction coefficient"  $S/N$  is a linear function of the normalized slip at the wall,

$$\frac{S}{N} = \frac{3}{7} \frac{1+\beta_0}{1+e} r, \quad (20)$$

where  $r$  is defined by (14). The flux is given by

$$\frac{Q}{N\sqrt{3T}} = \frac{3}{28(1+e)} [2(1+\beta_0)^2 r^2 - (1-\beta_0^2)] - \frac{3}{8} (1-e). \quad (21)$$

As expected, neither of these expressions depend upon  $\mu$ .

In the second asymptotic limit, sliding occurs for all particles and friction is small,  $\mu < \mu/\bar{\mu}_0$ , so all particles collide at angles such that  $\gamma < \gamma_0$ . It is the "small friction/all sliding" limit. Here, because the ratio of the tangential and normal components of  $\mathbf{J}^{(1)}$  is  $\mu$ , the ratio of the average of these components,  $S/N$ , also equals  $\mu$ ,

$$S/N = \mu. \quad (22)$$

In this limit, Jenkins calculates the flux

$$\frac{Q}{N\sqrt{3T}} = \frac{3}{8} [(7/2)(1+e)\mu^2 - (1-e)]. \quad (23)$$

Because all contacts are sliding in this limit, Eqs. (22) and (23) do not involve  $\beta_0$ .

For convenience, Jenkins normalizes the stress ratio by defining

$$R \equiv \frac{7}{2} \frac{1+e}{1+\beta_0} \frac{S}{N}, \quad (24)$$

so that  $R = 3r/2$  in the large friction/no sliding limit and  $R = \bar{\mu}_0$  in the small friction/all sliding limit.

### B. Low friction

Figures 2–4 illustrate our results for the variations of  $S/N$  with normalized slip at several values of the collision properties. Predictably, we find excellent agreement with Jenkins' theory in the limit where sliding occurs for all particles. Practically, this takes place at large values of the normalized slip, even though  $\mu$  is not always smaller than  $\mu/\bar{\mu}_0$ .

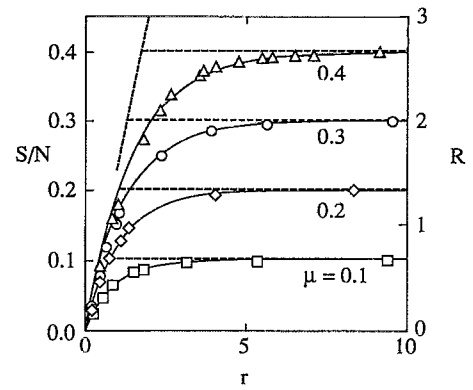


FIG. 2. Variations of the dynamic friction coefficient with friction for the conditions  $e=0.9$ ,  $\beta_0=0$ ,  $L_x/\sigma=L_y/\sigma=L_z/\sigma=5.9$ . The abscissa is the normalized slip from (14). The squares, diamonds, circles, and triangles are  $\mu=0.1, 0.2, 0.3$ , and  $0.4$ , respectively. The solid lines are the corresponding plots of (25). The oblique and horizontal dashed lines represent Jenkins' predictions in the large friction/no sliding and the small friction/all sliding limits, respectively. The right-hand axis shows the corresponding values of  $R$ .

In addition, for nearly elastic particles,  $e \geq 0.9$ , and for  $\mu > \mu/\bar{\mu}_0$ , our results agree well with an extrapolation of Jenkins' predictions in the large friction/no sliding limit to values of  $r$  below 1.

Remarkably, as Jenkins predicted,  $S/N$  is always lower than  $\mu$ . Thus at low values of the slip, because a majority of collisions do not involve sliding, the dynamic friction coefficient becomes much smaller than the value of  $\mu$  for individual particles. This mechanism may be relevant to phenomena such as avalanches and long run-out landslides, which appear to involve surprisingly low values of  $S/N$ .

In our simulations, we observe that  $S/N$  is relatively unaffected by the flow conditions in the interior. As Fig. 5 illustrates, substantial changes in  $L_y/\sigma$ ,  $\bar{v}$ , and  $\mu^p$  have a minimal effect on  $S/N$ . The only significant deviations are observed when the coefficient of normal restitution of interior particles is considerably reduced (Fig. 5, open circles). The changes in the structure of the flow associated with low values of  $e^p$  may be responsible for this effect (Hopkins,

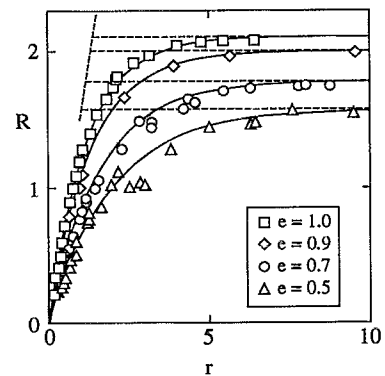


FIG. 3. Variations of the normalized dynamic friction coefficient with normal restitution for the conditions  $\mu=0.3$ ,  $\beta_0=0$ ,  $L_x/\sigma=L_y/\sigma=L_z/\sigma=5.9$ . The squares, diamonds, circles, and triangles are  $e=1.0, 0.9, 0.7, 0.5$ , respectively. The solid and dashed lines have the same meaning as in Fig. 2.

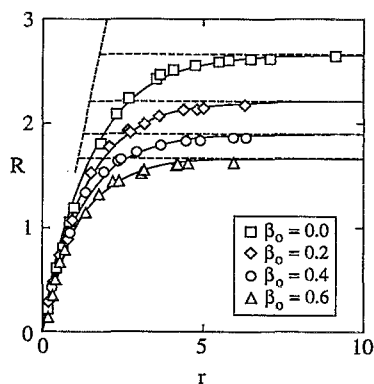


FIG. 4. Variations of the normalized dynamic friction coefficient with tangential restitution for the conditions  $e=0.9$ ,  $\mu=0.4$ ,  $L_x/\sigma=L_y/\sigma=L_z/\sigma=5.9$ . The squares, diamonds, circles, and triangles are  $\beta_0=0, 0.2, 0.4, 0.6$ , respectively. The solid and dashed lines have the same meaning as in Fig. 2.

Jenkins, and Louge).<sup>30</sup> In addition, steady flows may also be driven by a gravitational field in the direction of shear. In this case, instead of changing  $U/\sqrt{T_0}$ , we raise the strength of the field to produce increasing values of  $r$ . The resulting flows have similar characteristics than those without gravity; in particular, they exhibit the same dependence of  $S/N$  on  $r$ .

Therefore,  $S/N$  is generally a robust flow variable. As Jenkins implied, it is reasonable to assume that there is a general expression for  $S/N$  in terms of  $r$  and collision properties. However, despite the considerable insight that his theory brings, Jenkins is not in a position to generate such an expression. Because the latter is of interest in practical applications, we have produced it empirically by least-squares fitting five constants through the results of a matrix of 400 simulations with properties in the range  $0.5 \leq e \leq 1$ ,  $0.1 \leq \mu \leq 0.4$ , and  $0 \leq \beta_0 \leq 0.6$ . We obtain

$$(S/N) \approx \mu [1 - \exp(-ar/\mu)], \quad (25)$$

where the slope at low values of  $r$  is given by

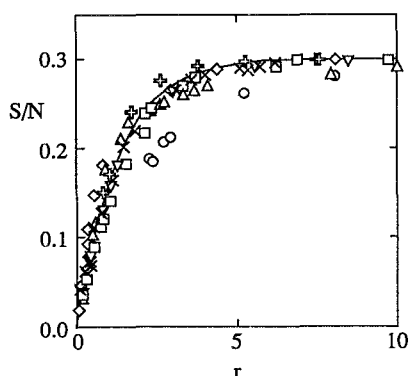


FIG. 5. Variations of the dynamic friction with conditions in the interior for  $e=0.9$ ,  $\mu=0.3$ ,  $\beta_0=0$ , and  $L_x/\sigma=L_y/\sigma=L_z/\sigma=5.9$ , unless otherwise noted. The solid line is Eq. (25). The squares and diamonds represent  $L_y/\sigma=11.7$  and  $22.3$ , respectively. The upward and downward triangles are  $\mu^p=0.1$  and  $0.6$ , respectively. The circles are  $e^p=0.2$ . The crosses are  $\bar{\nu}=45\%$ . The multiplication signs represent simulations with fixed  $U/\sqrt{T_0}=0.2$  that are driven by the gravity  $\phi$  in the direction of shear with  $3.10^{-4} \leq \phi\sigma/T_0 \leq 0.06$ .

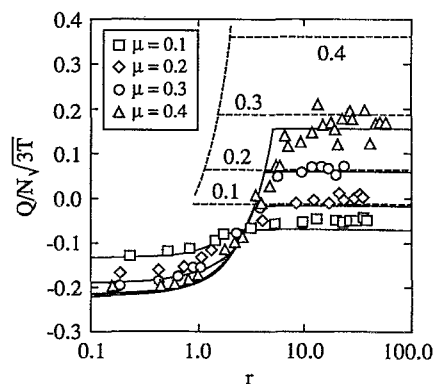


FIG. 6. Variations of the normalized flux of fluctuation energy with friction. The symbols and conditions are the same as in Fig. 2. The solid lines are the corresponding plots of Eqs. (28) and (29). The oblique and horizontal dashed lines are the predictions of Jenkins in the large friction/no sliding and the small friction/all sliding limits, respectively.

$$a \approx a_1 \exp[-a_2(1-e)][1 - \exp(-a_3\mu)](1+\beta_0)^{a'}, \quad (26)$$

and the exponent  $a'$  is approximately

$$a' \approx a_4[1 - \exp(-a_5\mu)]. \quad (27)$$

The best constants are  $a_1 \approx 0.3537$ ,  $a_2 \approx 1.042$ ,  $a_3 \approx 4.453$ ,  $a_4 \approx 2.068$ , and  $a_5 \approx 0.8468$ . The choice of constants and exponential functions in Eqs. (25)–(27) is arbitrary. Its only justification is that it provides an excellent fit through the simulation data for a wide range of collision properties.

Figures 6–8 show typical results for the normalized flux of fluctuation energy. Like Jenkins, we distinguish two asymptotic limits. In the first, all particles slide upon contact with the wall. There, the normalized flux is constant. Although the values of  $\mu$  employed in the simulations are not always smaller than  $\mu/\bar{\mu}_0$ , the theory in the small friction/all sliding limit [Eq. (23)] captures the trends observed here. In fact, quantitative agreement with theory improves with decreasing  $\mu$ .

In addition, the large friction/no sliding limit of Jenkins' theory also captures the principal trends observed at low val-

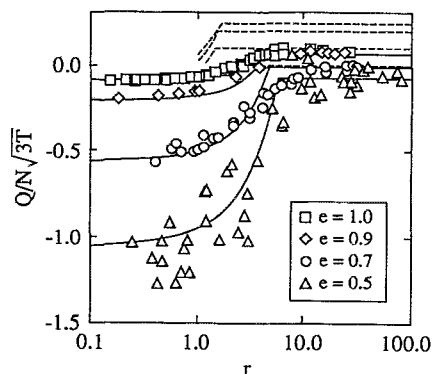


FIG. 7. Variations of the normalized flux of fluctuation energy with normal restitution. The symbols and conditions are the same as in Fig. 3. The solid and dashed lines have the same meaning as in Fig. 6.

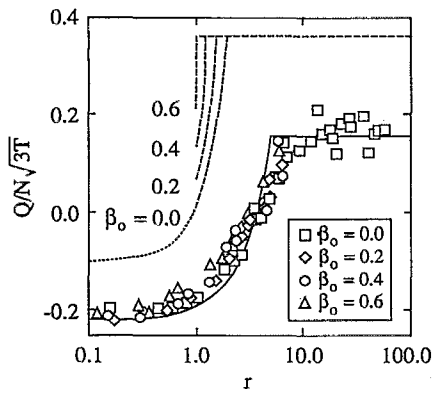


FIG. 8. Variations of the normalized flux of fluctuation energy with tangential restitution. The symbols and conditions are the same as in Fig. 4. The solid and dashed lines have the same meaning as in Fig. 6. The dotted line is an extrapolation to  $r < 1$  of Jenkins' equation (21) for  $\beta_0 = 0$ .

ues of the slip when  $\mu > \mu/\bar{\mu}_0$ . However, the dependence of the flux on  $\beta_0$  is less pronounced than Jenkins' prediction in this limit. Our experience is that the contribution of sliding collisions dominates the flux even at small values of the slip. Consequently, as Fig. 8 illustrates, the effect of tangential restitution is minimal for finite friction.

As in the case of the dynamic friction coefficient, we find that the normalized energy flux is a robust flow variable that is not greatly affected by parameters other than the normalized slip and the collision properties of the wall. Nevertheless, because the flux is a moment of higher order than the dynamic friction, it is more subject to noise. In particular, we observe that simulations with wider Couette cells ( $L_y/\sigma = 12, 22$ ) typically exhibit greater uncertainties than those conducted in narrower channels. As Fig. 9 indicates, within that uncertainty, the values of  $Q/N\sqrt{3T}$  are relatively unaffected by the restitution coefficient of interior particles, the width of the Couette domain, the value of  $\bar{\nu}$ , and the presence of a gravitational field. The only substantial deviations are observed when the coefficient of friction of interior particles is much lower than that of the wall (upward triangles in Fig. 9).

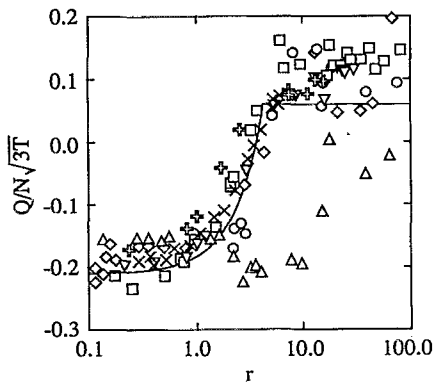


FIG. 9. Variations of the normalized flux of fluctuation energy with conditions in the interior for  $e = 0.9$ ,  $\mu = 0.3$ ,  $\beta_0 = 0$ , and  $L_x/\sigma = L_y/\sigma = L_z/\sigma = 5.9$ , unless otherwise noted. The symbols have the same meaning as in Fig. 5.

Consequently, as with dynamic friction, we propose an empirical fit of the normalized flux for properties in the range  $0.5 \leq e \leq 1$ ,  $0.1 \leq \mu \leq 0.4$ , and  $0 \leq \beta_0 \leq 0.6$ . Unlike Eq. (25), we cannot find a simple function that is continuously valid in the two asymptotic limits. Instead, we suggest two expressions. The first applies to low values of the slip,

$$\lim_{r \rightarrow 0} \frac{Q}{N\sqrt{3T}} \approx B_1 r^2 + B_2 r - B_3, \quad (28)$$

where  $B_1 \approx b_1/(1+e)$ ,  $B_2 \approx b_2(1-e)[1 - \exp(-b_3\mu)]$ , and  $B_3 \approx B_4[1 - \exp(-B_5\mu)]$ . We find  $B_4 \approx b_4(1-e)^2 + b_5(1-e) + b_6$ , and  $B_5 \approx b_7(1-e) + b_8$ . The constant providing the best fit are  $b_1 \approx 0.02$ ,  $b_2 \approx 0.3$ ,  $b_3 \approx 3.4$ ,  $b_4 \approx 1.8$ ,  $b_5 \approx 1.1$ ,  $b_6 \approx 0.1$ ,  $b_7 \approx 4.6$ , and  $b_8 \approx 8.6$ . Note that, because our results do not exhibit any significant dependence of the flux on tangential restitution, we have ignored  $\beta_0$  in (28). In the limit of infinite friction, the fit has a similar form than Jenkins' expression (21) in the large friction/no sliding limit with  $\beta_0 = 0$ . There, Jenkins obtains  $b_1 = 3/14$ ,  $B_2 = 0$ , and  $B_3 = B_4 = 3/28(1+e) + 3(1-e)/8$ .

For large values of the slip, the constant flux is well represented by

$$\lim_{r \rightarrow \infty} \frac{Q}{N\sqrt{3T}} \approx d_1(1+e)\mu^2 + d_2(1-e)\mu - d_3(1-e), \quad (29)$$

where  $d_1 \approx 0.522$ ,  $d_2 \approx 2.57$ , and  $d_3 \approx 1.08$ . For comparison, Jenkins' theory predicts  $d_1 = 21/16$ ,  $d_2 = 0$ , and  $d_3 = 3/8$  [Eq. (23)]. The additional terms that we introduce in (28) and (29) may be due to the dependence of the flux on rotational temperature, which Jenkins has not fully incorporated in the theory.

Again, we emphasize that Eqs. (28) and (29) are not meant to generate any particular physical insight. In the absence of a quantitative theory, they merely provide empirical expressions that may be used as practical boundary conditions for the flux over a convenient range of collision properties.

### C. Intermediate friction

In addition to his calculations in the large friction/no sliding and small friction/all sliding limits, Jenkins also evaluates  $S/N$  and  $Q/N\sqrt{3T}$  in the intermediate cases where friction is large, but there is either small or large sliding. Because sliding is possible, these cases involve practical values of  $\mu$  larger than  $\mu/\bar{\mu}_0$ , yet smaller than approximately 1.5, beyond which, in our experience, fewer than 10% of all collisions involve sliding. In this interval, we find that, as  $\mu$  increases, the behaviors of  $S/N$  and  $Q/N\sqrt{3T}$  change progressively in ways that are not anticipated by the theory.

Figure 10 illustrates this effect for the dynamic friction coefficient. Surprisingly, although the empirical expressions (25) to (27) were obtained from simulations with  $0.1 \leq \mu \leq 0.4$ , they remain valid at low  $r$  for any  $\mu > 0.4$  (dashed lines, Fig. 10). However, for  $\mu > 0.6$ , large values of the slip become increasingly impossible to achieve. Instead, as  $U/\sqrt{T_0}$  is increased, the normalized slip reaches a maximum, then decreases again.



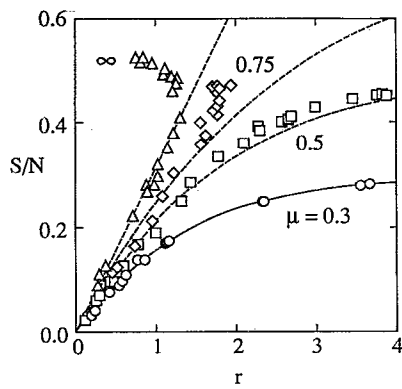


FIG. 10. Transition of the dynamic friction between the low and high friction regimes. The conditions are  $e=0.9$ ,  $\beta_0=0$ ,  $L_x/\sigma=L_z/\sigma=5.9$ . The circles, squares, and diamonds are  $L_y/\sigma=5.9$ , and  $\mu=0.3$ ,  $0.5$ , and  $0.75$ , respectively. The triangles are  $L_y/\sigma=22.3$  and  $\mu=\infty$ . The lines are the corresponding plots of (25).

As Fig. 11 indicates, we observe a similar bifurcation of the flux around  $\mu \approx 0.6$ . For  $\mu < 0.6$ , the flux is well described by the empirical expressions (28) and (29). For  $\mu \geq 0.6$ , as the boundary becomes considerably more dissipative with increasing values of  $U/\sqrt{T_0}$ , the flux progressively exhibits an altogether different behavior. We discuss this phenomenon next.

#### D. High friction

In this section, we focus on flows with values of  $\mu$  large enough that no collisions involve sliding. Although the same results may be obtained with any  $\mu \geq 1.5$ , the present simulations assume an infinite value of  $\mu$ , so the collisional impulse is always  $J^{(2)}$ , and all results are independent of friction.

In the high friction regime, arbitrarily large values of the normalized slip at the point of contact cannot be achieved. The reason is that, unlike low friction, the absolute spin magnitude of the particles adjacent to the wall continues to grow with increasing  $U/\sqrt{T_0}$  (Fig. 12). Then, at a large enough

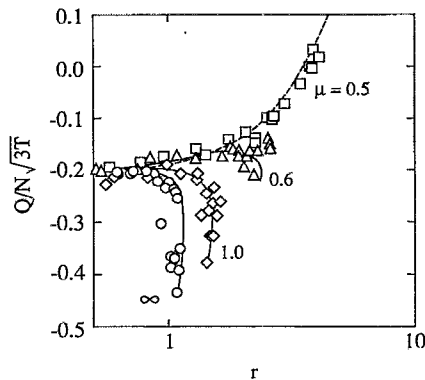


FIG. 11. Transition of the normalized flux of fluctuation energy. The squares, triangles, diamonds, and circles are  $\mu=0.5$ ,  $0.6$ ,  $1$ , and  $\infty$  with  $L_x/\sigma=L_y/\sigma=L_z/\sigma=5.9$ . The dashed line is a plot of (28) for  $\mu=0.5$ . The solid lines are visual fits through the data at higher  $\mu$ .

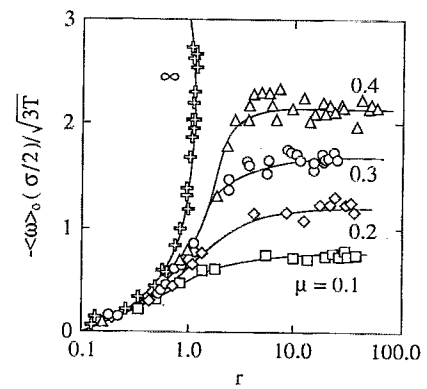


FIG. 12. Normalized magnitude of the mean spin at the wall in the  $z$  direction versus normalized slip for the conditions  $e=0.9$ ,  $\beta_0=0$ ,  $L_x/\sigma=L_y/\sigma=L_z/\sigma=5.9$ . The squares, diamonds, circles, triangles, and crosses are  $\mu=0.1$ ,  $0.2$ ,  $0.3$ ,  $0.4$ , and  $\infty$ , respectively.

value of  $U/\sqrt{T_0}$ , the contribution of the spin to the mean velocity of the contact point begins to grow faster than that of the mean velocity of the center of mass. Consequently, because at the wall in the direction of shear

$$g_0 = \langle c \rangle_0 + (\sigma/2) \langle \omega \rangle_0, \quad (30)$$

where  $\langle \omega \rangle_0$  is negative,  $g_0$  begins to decrease. This reversal of the mean slip of the contact point creates two branches in the curves of  $S/N$  and  $Q/N\sqrt{3T}$  vs  $r$ . Thus for a given value of  $r$ , there are generally two possible values of the dynamic friction and the normalized flux. However, as Fig. 13 indicates,  $S/N$  grows monotonically with the normalized mean velocity of the center of mass.

Therefore, at increasing values of the mean shear, particles of high friction tend towards a limit where they roll without slipping. Because it ignores enduring contacts, our simulation can only approach this limit, and thus it cannot achieve the arbitrarily large values of  $\langle c \rangle_0$  that rolling

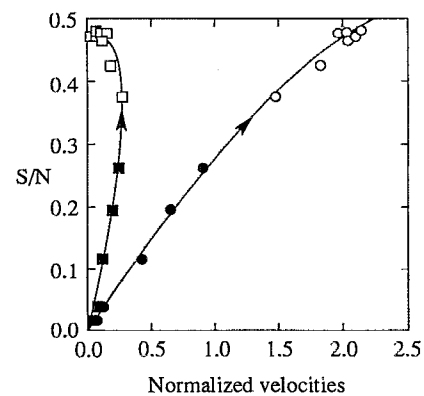


FIG. 13. Dynamic friction versus normalized velocities  $g_0/\sqrt{3T}$  (squares) and  $\langle c \rangle_0/\sqrt{3T}$  (circles) for the conditions  $e=0.8$ ,  $\mu=\infty$ ,  $\beta_0=0.8$ ,  $L_x/\sigma=L_y/\sigma=L_z/\sigma=5.9$ . The former velocity is the normalized slip at the contact point, and the latter is the normalized mean velocity of the center of mass of particles touching the wall. The open and filled symbols represent the upper and lower branches of the  $S/N$  versus  $r$  curve, respectively. The solid lines are visual fits through the data. The arrows indicate the direction of increasing  $U/\sqrt{T_0}$ .

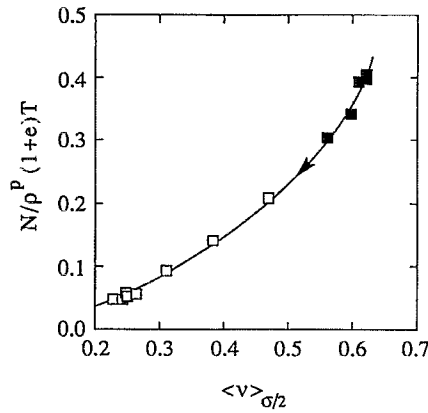


FIG. 14. Dimensionless normal stress versus mass-averaged particle volume fraction evaluated at a distance  $\sigma/2$  from the wall. The conditions are those of Fig. 13. The solid line is a visual fit through the data. The arrows indicate the direction of increasing  $U/\sqrt{T_0}$ . The filled symbols represent the conditions in the lower branch of the  $S/N$  versus  $r$  curve.

spheres may eventually exhibit at high mean shear rates. A soft particle simulation like that of Walton and Braun<sup>31</sup> would be more appropriate in this case.

Figure 14 is a plot of the dimensionless normal stress against the mass-averaged particle volume fraction evaluated at a distance  $(\sigma/2)$  from the wall. Here the stress is normalized with  $\rho^p$ , the material density of the particles, and  $T$ . Figures 12–14 show that in the lower branch of the  $S/N$  curve, the flow is characterized by a relatively high normal stress, a large particle volume fraction at the wall, and a low spin. In the upper branch, the normal stress and volume fraction are smaller and the spin is greater.

Figures 15 and 16 illustrate the dependence of the dynamic friction coefficient on tangential and normal restitution, respectively. Surprisingly, we find that an extrapolation of our empirical expressions (25) to (27) to infinite friction captures reasonably well  $S/N$  in the lower branch of the curve. Similarly, an extrapolation of Jenkins' predictions to

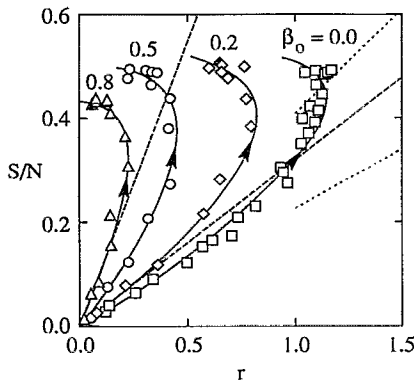


FIG. 15. Variations of  $S/N$  with tangential restitution in the high friction regime. The conditions are  $\mu = \infty$ ,  $e = 0.9$ , and  $L_x/\sigma = L_y/\sigma = L_z/\sigma = 5.9$ . The squares, diamonds, circles, and triangles are  $\beta_0 = 0, 0.2, 0.5$ , and  $0.8$ , respectively. The solid lines are visual fits through the data. The arrows have the same meaning as in Fig. 13. The dashed lines are (25) with  $\mu = \infty$ ,  $e = 0.9$ , and  $\beta_0 = 0$  and  $0.8$ . The dotted lines are the corresponding predictions of Jenkins in the large friction/no sliding limit.

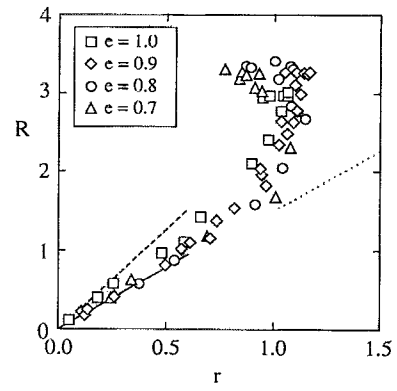


FIG. 16. Variations of  $R$  with normal restitution. The conditions are  $\mu = \infty$ ,  $\beta_0 = 0$ , and  $L_x/\sigma = L_y/\sigma = L_z/\sigma = 5.9$ . The squares, diamonds, circles, and triangles are  $e = 1, 0.9, 0.8, 0.7$ , respectively. The solid and dashed slopes represent (25) with  $\mu = \infty$ ,  $\beta_0 = 0$ , and  $e = 0.7$  and  $1$ , respectively. The dotted line is the prediction of Jenkins in the large friction/no sliding limit.

values of  $r < 1$  agrees well with our results for  $\beta_0 = 0$ . However, significant departures from the theory are observed for  $\beta_0 > 0$ . Figure 17 shows that in the high friction regime,  $S/N$  is again a robust flow parameter, which depends very little on the conditions of the simulations. The only significant departure from a relatively universal dependence of  $S/N$  on  $r$  occurs when the coefficient of friction of interior particles is very small. Figures 18–20 show the corresponding dependence of the normalized flux on  $\beta_0$ ,  $e$  and conditions in the interior. Again, we find that  $Q/N\sqrt{3T}$  is robust, unless  $\mu^p$  is very small.

#### IV. ASSUMPTIONS OF THE THEORY

In this section, we examine the assumptions of Jenkins' theory in the light of our results.

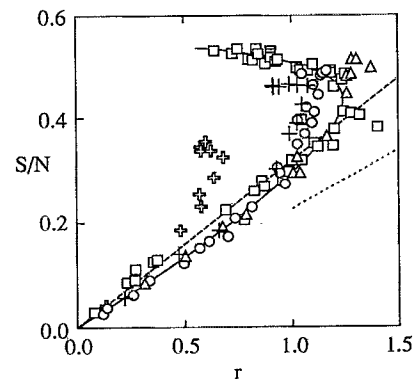


FIG. 17. Variations of the dynamic friction with conditions in the interior for  $e = 0.9$ ,  $\mu = \infty$ ,  $\beta_0 = 0$ , and  $L_x/\sigma = L_y/\sigma = L_z/\sigma = 5.9$ . The circles and the squares are  $L_y/\sigma = 5.9$  and  $22.3$ , respectively. The triangles represent simulations driven by the gravity  $\phi$  in the direction of shear, with  $U/\sqrt{T_0} = 0.2$  and  $7.10^{-4} \leq \phi\sigma/T_0 \leq 0.14$ . The crosses and plus signs are  $\mu^p = 0.1$  and  $0.5$ , respectively. The solid line is a visual fit through the data. The dashed and dotted lines are, respectively, a plot of (25) and the prediction of Jenkins in the "large friction/no sliding" limit with  $e = 0.9$ ,  $\beta_0 = 0$ , and  $\mu = \infty$ .

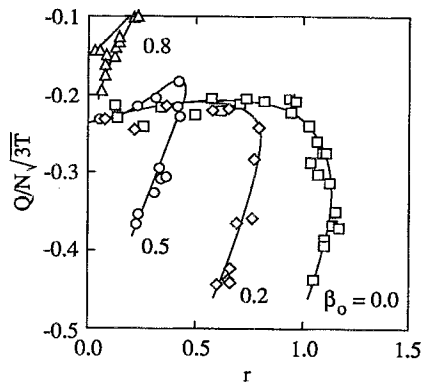


FIG. 18. Variation of the normalized flux of fluctuation energy with tangential restitution. The conditions and symbols are found in Fig. 15.

### A. Spin temperature

In order to facilitate the integrations for  $\mathbf{M}$  and  $D$ , Jenkins ignores the fluctuations in angular velocities, or  $\tau=0$ . Nevertheless, as Fig. 21 indicates, the rotational temperature may be substantial, particularly when the slip increases. Thus it is possible that the failure of the theory to produce a quantitative prediction of the flux arises from its incomplete treatment of the rotational temperature.

### B. Velocity distribution

In order to render his calculations tractable, Jenkins adopts an isotropic velocity distribution function such that the magnitudes of the fluctuation velocities equal their root mean square,

$$f(\mathbf{c}, \omega) = F(C^2) = \frac{n^*}{4\pi(3T)} \delta(C^2 - 3T), \quad (31)$$

where  $\delta(\cdot)$  is the delta function. Because the distribution function is used to evaluate the collisional rate of change at the wall, it concerns only particles experiencing wall collisions. Thus in order to test Jenkins' distribution, we construct a histogram of the velocities of a large number of particles involved in such collisions.

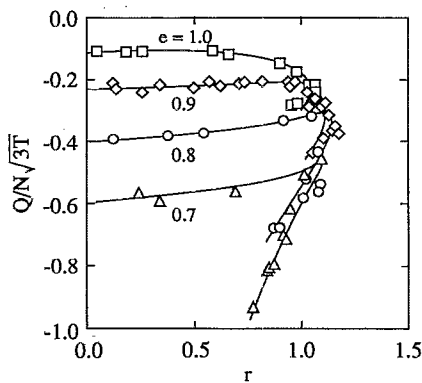


FIG. 19. Variation of the normalized flux of fluctuation energy with normal restitution. The conditions and symbols are found in Fig. 16. The solid lines are visual fits through the data.

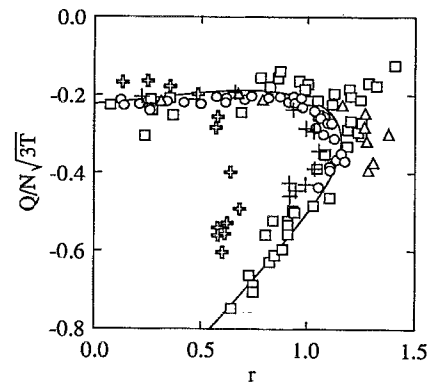


FIG. 20. Variations of the normalized flux of fluctuation energy with conditions in the interior. The symbols and conditions are found in Fig. 17.

To this end, we divide a portion of the velocity space centered at the mean particle velocity into a three-dimensional Cartesian array of  $41 \times 41 \times 41$  rectangular bins. The widths  $\lambda_\gamma$  of these bins in the three Cartesian direction  $\gamma=x,y,z$  is one-tenth of the standard deviation  $s_\gamma$  of the velocity in that direction,  $\lambda_\gamma = s_\gamma/10$ . When a particle collides anywhere with the wall, we record its velocities immediately before ( $\mathbf{c} \cdot \mathbf{n} < 0$ ), and immediately after ( $\mathbf{c}' \cdot \mathbf{n} > 0$ ), the collision. We increment the number  $\epsilon(i,j,k)$  of particles with velocity falling in each bin of index  $(i,j,k)$  until  $N_c$  particles have collided with the wall. In the present simulations, the bins have indices  $-20 \leq i \leq 20$ ,  $-20 \leq j \leq 20$ ,  $-20 \leq k \leq 20$ , and  $N_c = 2 \cdot 10^5$ .

For simplicity, we normalize our velocity histogram using

$$\phi(i,j,k) = \left( \frac{(3T)^{3/2}}{\lambda_x \lambda_y \lambda_z} \right) \frac{\epsilon(i,j,k)}{N_c}, \quad (32)$$

and we make the fluctuating velocities dimensionless through  $\sqrt{3T}$ . Therefore, the sum of  $\phi$  over the entire dimensionless velocity space is one.

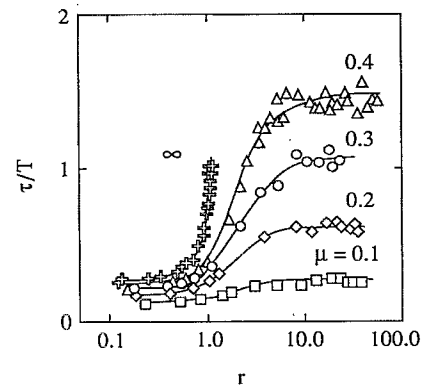


FIG. 21. Variations of the ratio of the spin and translation temperatures with friction. The squares, diamonds, circles, triangles, and crosses are  $\mu=0.1, 0.2, 0.3, 0.4$ , and  $\infty$ , respectively. The conditions are  $e=0.9$ ,  $\beta_0=0$ , and  $L_x/\sigma=L_y/\sigma=L_z/\sigma=5.9$ . The solid lines are visual fits through the data.

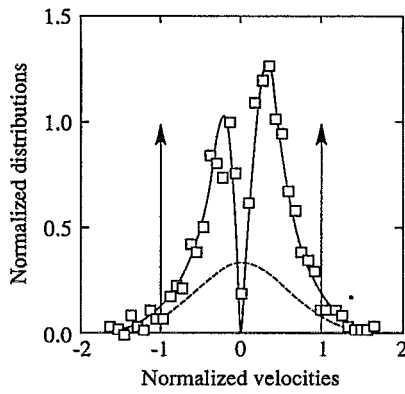


FIG. 22. Section of the normalized velocity distribution function  $\phi$  along the plane  $C_x=C_z=0$  for the conditions  $e=0.9$ ,  $\mu=0.3$ ,  $\beta_0=0$ ,  $L_x/\sigma=L_y/\sigma=L_z/\sigma=5.9$ , and  $r=0.65$ . The solid line is a visual fit through the data. The dashed line is the corresponding Maxwellian distribution. The arrows represent the delta function employed by Jenkins.

$$\sum_{i,j,k=-\infty}^{+\infty} \phi(i,j,k) \left( \frac{\lambda_x \lambda_y \lambda_z}{(3T)^{3/2}} \right) = 1, \quad (33)$$

rather than the number density. This unusual normalization permits us to focus on the velocity distribution at the wall without considering the spatial distribution there. In this formulation, we compare  $\phi$  with the function  $F(C^2)(3T)^{3/2}/n^*$  postulated by the theory. For a typical flow involving nearly elastic particles, Fig. 22 shows the variations of  $\phi$  vs  $C_y/\sqrt{3T}$  with  $C_x=C_z=0$ . In this graph, negative velocities are those of particles about to collide with the wall. Because in order to experience a collision there, particles must travel toward the wall, the probability of a zero velocity component in the direction  $z$  normal to the wall vanishes, and the distribution exhibits two maxima. Consequently, the Maxwellian does not adequately describe the distribution of velocities normal to the wall. However, because the wall does not obstruct the flow in the  $x$  and  $z$  directions, the variations of the histogram with  $C_x/\sqrt{3T}$  (squares) and  $C_z/\sqrt{3T}$  (circles) are symmetrical and bell shaped (Fig. 23).

For nearly elastic particles, the  $y$  component of the second moments of the velocity fluctuations is greater than the other two. Because in an unbounded flow the velocity distribution of such particles would be isotropic, this anisotropy is probably due to the presence of the wall. As Fig. 24 indicates, it disappears with increasing values of the slip. However, as the coefficient of normal restitution decreases, an anisotropy similar to that studied by Jenkins and Richman<sup>32</sup> for smooth disks competes with the anisotropy associated with the wall. Here, with increasing values of  $r$ , the component of the second moment in the direction of shear progressively dominates the component normal to the wall. In addition, we observe that the histogram of inelastic particles is considerably narrower in the direction normal to the wall. This effect probably results from the significantly lower velocities that inelastic particles acquire after colliding with the wall.

Using a normalization similar to (32) but based on the rotational temperature  $\tau$ , we calculate the dimensionless his-

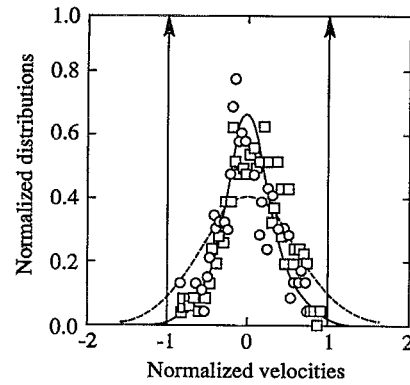


FIG. 23. Sections of the normalized velocity distribution function  $\phi$  along the planes ( $C_x/\sqrt{3T}=0$ ,  $C_y/\sqrt{3T}=-0.57$ ) (circles) and ( $C_x/\sqrt{3T}=0$ ,  $C_y/\sqrt{3T}=-0.57$ ) (squares) for the conditions of Fig. 22. The value  $C_y/\sqrt{3T}=-0.57$  is the normalized mean velocity of the particles about to collide with the wall. The meaning of the lines is found in Fig. 22.

tograms of the angular velocity fluctuations. The corresponding distribution is typically anisotropic, bell shaped and narrower than the Maxwellian in the  $x$  and  $y$  directions. It exhibits a larger variance in the  $z$  direction of the mean particle spin. Figure 24 shows that this anisotropy of the spin fluctuations increases with increasing values of  $r$  and with increasing friction. However, it depends weakly on the coefficient of normal restitution.

Figure 25 shows typical profiles of the normalized, mass-averaged second moments of the velocity fluctuations  $\langle C_\alpha^2 \rangle / 3T$  and the spin fluctuations  $\langle \Omega_\alpha^2 \rangle / 3T$  in the three directions  $\alpha=x,y,z$ . Although considerably more noisy, the corresponding center-average profiles have nearly the same form. As this figure indicates, the anisotropy of these moments is considerably different at the wall than it is in the interior. Clearly, the velocity distribution at the wall should not be inferred from that of an unbounded flow. However, it appears that the anomalous anisotropy of the second mo-

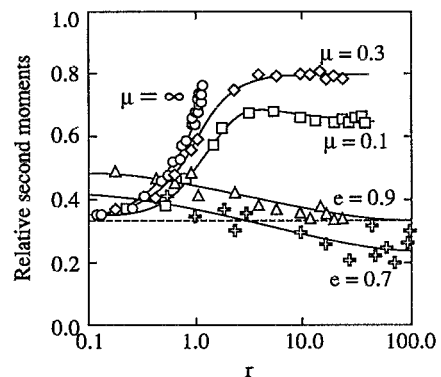


FIG. 24. Anisotropy of the mass-averaged second moments of the velocity fluctuations at the wall for the conditions  $\beta_0=0$  and  $L_x/\sigma=L_y/\sigma=L_z/\sigma=5.9$ . The triangles and crosses represent  $\langle C_x C_y \rangle / [\langle C_x C_x \rangle + \langle C_y C_y \rangle + \langle C_z C_z \rangle]$  for the conditions  $\mu=0.3$ , and  $e=0.9$  and  $0.7$ , respectively. The squares, diamonds, and circles are  $\langle \Omega_x \Omega_x \rangle / [\langle \Omega_x \Omega_x \rangle + \langle \Omega_y \Omega_y \rangle + \langle \Omega_z \Omega_z \rangle]$  for  $e=0.9$ ,  $0.3$ , and  $\infty$ , respectively. The solid lines are visual fits through the data. Isotropic second moments would lie on the horizontal dashed line.

ments is primarily confined within the first layer of particles away from the wall ( $0 \leq y/\sigma \leq 1$ ). These results agree qualitatively with Drake's observations of acetate spheres in a bumpy, two-dimensional chute.<sup>33</sup>

### C. Spatial distribution

The presence of the wall affects the spatial distribution of spheres in its vicinity. As Fig. 26 illustrates, oscillations of the local volume fraction persist several diameters in the interior. Their character depends strongly on the form of the averaging. Because the particles cannot penetrate the wall, the fraction of the volume that they occupy there is zero.

If mass-averaging is employed, geometry requires that the first peak of the volume fraction be located at a distance  $y \geq (\sigma/2)$  from the wall [Fig. 26(a)]. In fact, our experience shows that the first peak lies near  $y = \sigma/2$ . Its magnitude represents the average two-dimensional packing of spheres adjacent to the wall.

In contrast, while it vanishes for  $y < \sigma/2$ , the center-averaging produces greater values of the local volume fraction at  $y = \sigma/2$  [Fig. 26(b)]. (In the extreme, a regular array of spheres touching the wall would create a series of evenly spaced delta functions  $\delta[y - \sigma(i + 1/2)]$  with  $i \in \mathbb{N}$ .) In typical granular flows, the random placement of spheres widens the first peak to produce a finite value of the local volume fraction at  $y = \sigma/2$ .

By treating the wall as a sphere of infinite radius, Henderson, Abraham, and Barker<sup>34</sup> (HAB) extend the Percus–Yevick theory<sup>35</sup> and predict the spatial distribution function  $g_{12}$  in the presence of a random array of spheres with constant volume fraction  $\nu^*$  in the bulk,

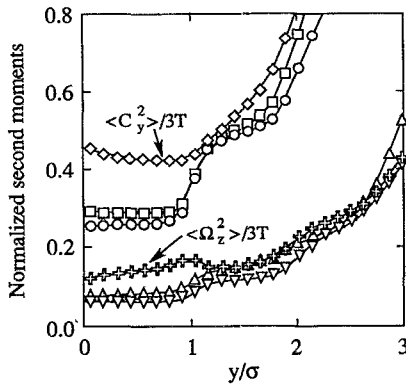


FIG. 25. Profiles of the normalized, mass-averaged second moments of velocity fluctuations for the conditions of Fig. 22. The squares, diamonds, and circles represent  $\langle C_x C_x \rangle / 3T$ ,  $\langle C_y C_y \rangle / 3T$  and  $\langle C_z C_z \rangle / 3T$ , respectively. The upward triangles, downward triangles, and crosses are  $\langle \Omega_x \Omega_x \rangle / 3T$ ,  $\langle \Omega_y \Omega_y \rangle / 3T$ , and  $\langle \Omega_z \Omega_z \rangle / 3T$ , respectively.

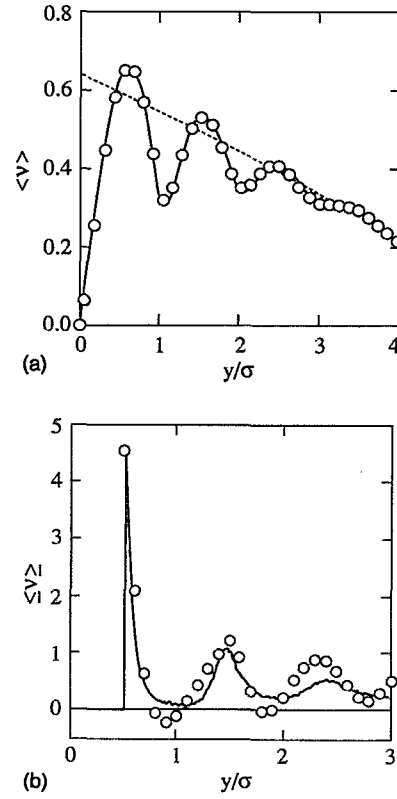


FIG. 26. Profiles of local volume fraction with relative distance from the wall for the conditions of Fig. 22. (a) Mass-average  $\langle \nu \rangle$ ; the circles are the simulation data; the solid line is a visual fit through these; the dashed line is a visual extrapolation of  $\nu^*$  from the interior to the wall. (b) Center-average  $\langle \nu \rangle$ ; the solid line is the simulation data averaged over ten consecutive runs; the circles are theoretical predictions of the HAB theory that matches the measured  $\langle \nu \rangle$  at  $y = \sigma/2$  using  $\nu^* = 51.8\%$ .

$$g_{12}(\zeta) = \frac{1+2\nu^*}{(1-\nu^*)^2} - \frac{3}{5} \nu^* \frac{10-2\nu^*+\nu^{*2}}{1+2\nu^*} \alpha_1 \zeta$$

$$+ \frac{1}{5} \nu^* (3\theta_1 + 2\theta_2) + 12\nu^* \int_0^\zeta t [\alpha_1(t-\zeta) + \theta_1 + \theta_2]$$

$$\times h_{11}(t) dt + 12\nu^* \int_\zeta^{1+\zeta} t (\zeta + 1 - t)^3$$

$$\times [\theta_1 + \theta_2(\zeta + 1 - t)] h_{11}(t) dt, \quad (34)$$

where

$$h_{11}(t) = g_{11}(t) - 1,$$

$$\zeta = (y/\sigma) - (1/2),$$

$$\alpha_1 = (1+2\nu^*)^2 / (1-\nu^*)^4,$$

$$\theta_1 = -2\nu^* (1+\nu^*/2) (1+2\nu^*) / (1-\nu^*)^4,$$

and

$$\theta_2 = \nu^* \alpha_1 / 2.$$

The function  $g_{11}(t)$  is the Percus–Yevick radial distribution function for a hard sphere, where  $1 \leq t < +\infty$  is the relative distance between the sphere centers.<sup>36</sup> From (34), the first peak of  $g_{12}$  located at  $\zeta=0$  has the magnitude

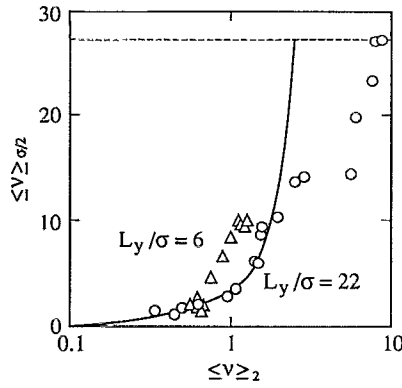


FIG. 27. Magnitude of the first peak of the center-averaged volume fraction profile  $\leq \nu \geq_{\sigma/2}$  versus that of the second peak  $\leq \nu \geq_2$ . The circles are  $e=0.9$ ,  $\mu=\infty$ ,  $\beta_0=0$ ,  $L_y/\sigma=22.3$ , and  $L_x/\sigma=L_z/\sigma=5.9$ . The triangles are  $e=0.7$ ,  $\mu=\infty$ ,  $\beta_0=0$ , and  $L_x/\sigma=L_y/\sigma=L_z/\sigma=5.9$ . The solid line is the corresponding prediction of the HAB theory for  $\nu^* g_{12}(0)$  vs  $\nu^* g_{12}(\zeta_2)$  from (35) and (36). The dashed line represents the theoretical upper bound for  $\leq \nu \geq_{\sigma/2}$  using  $\nu^* = \pi\sqrt{2}/6$ .

$$g_{12}(0) = [(1 + 2\nu^*) / (1 - \nu^*)^2], \quad (35)$$

and the local value of the volume fraction there is  $\leq \nu \geq_{\sigma/2} = \nu^* g_{12}(0)$ . The theoretical magnitude of the second peak has no such simple analytical form. Our numerical integrations of (34) indicate that it is well represented by the empirical fit

$$g_{12}(\zeta_2) \approx 1 + 14.1 \nu^{*3.44} \quad \text{for } 0.05 \leq \nu^* \leq 0.50, \\ 0.24 + 4.2 \nu^* \quad \text{for } 0.55 \leq \nu^* < \pi\sqrt{2}/6, \quad (36)$$

and that its location is approximately  $\zeta_2 \approx 1 + 1.89 [\pi\sqrt{2}/6 - \nu^*]^{3.14}$  for  $0.05 \leq \nu^* < \pi\sqrt{2}/6$ . It is intriguing to notice that the theoretical value  $g_{12}(\zeta_2)$  exhibits a change of slope at a value of  $\nu^*$  near the glass transition for hard spheres.

As Figs. 26(b) and 27 indicate, the HAB theory generally captures well the relative magnitude of the first two peaks of the spatial distribution function, even though the bulk volume fraction  $\nu^*$  is not constant across our flows. However, we note in Fig. 26(b) that the predictions of  $g_{12}$  occasionally become negative for relatively high values of  $\nu^*$ , which is unphysical. In addition, the theory becomes inadequate if the domain is too narrow (e.g.,  $L_y/\sigma \approx 6$ ) or if the magnitude of  $\nu^*$  is too large (Fig. 27). In the former case, the influence of the top boundary is probably too great to treat the domain above the flat wall as semi-infinite. In the latter, the flow at the wall may undergo a phase transition to a volume fraction beyond which the theory is not expected to succeed. Further effects associated with this phase transition are discussed later.

#### D. Collision integral

The spatial distribution function prescribes the local value of the volume fraction that enters the collision integral (15). For any velocity distribution function, the boundary traction in the direction normal to the wall is obtained by combining (15) and the normal component of (7) or (11),

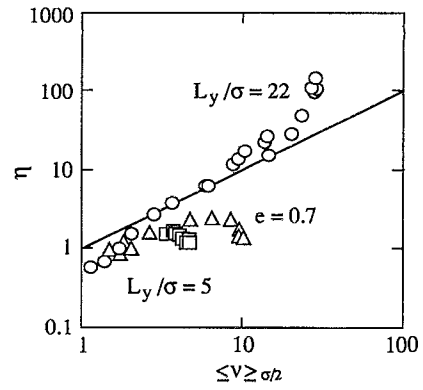


FIG. 28. Relative normal stress  $\eta$  versus  $\leq \nu \geq_{\sigma/2}$ . Triangles are  $e=0.7$ ,  $\mu=\infty$ ,  $\beta_0=0$ ,  $L_x/\sigma=L_y/\sigma=4.8$ ,  $L_z/\sigma=5.3$ ; squares are  $e=0.9$ ,  $\mu=0.3$ ,  $\beta_0=0$ ,  $L_x/\sigma=L_y/\sigma=4.8$ ,  $L_z/\sigma=5.3$ ; circles, see Fig. 27. The straight line represents  $\eta = \leq \nu \geq_{\sigma/2}$ .

$$N = \mathbf{M} \cdot \mathbf{n} = -g_{12}(0) \int \int \mathbf{J} \cdot \mathbf{n} f(\mathbf{c}, \omega) \mathbf{c} \cdot \mathbf{n} d\mathbf{c} d\omega \\ = g_{12}(0) n^* m (1 + e) \langle (\mathbf{c}^- \cdot \mathbf{n})^2 \rangle \\ = g_{12}(0) \nu^* \rho^p (1 + e) \langle C_y^- C_y^- \rangle, \quad (37)$$

where the integration is over all values of  $\mathbf{c}$  for which  $\mathbf{c} \cdot \mathbf{n} \leq 0$ , so  $C_y^-$  is the normal component of the particle velocity  $\mathbf{c}^-$  before the collision. In the spirit of the HAB theory, we have replaced Jenkins' factor  $\chi$  in (15) by  $g_{12}(0)$  in (37). We evaluate  $\langle C_y^- C_y^- \rangle$  using the center average  $\leq C_y^- C_y^- \geq$  for spheres about to impact the wall. The product  $g_{12}(0) \nu^*$  is the first peak of the local, center-averaged volume fraction  $\leq \nu \geq_{\sigma/2}$  evaluated at  $y/\sigma = 1/2$  or  $\zeta = 0$ . We note that if the velocity distribution was isotropic, then  $\langle C_y^- C_y^- \rangle$  would equate  $(1/2) \langle C_y^2 \rangle = T/2$  and (37) would reduce to the expression for the normal stress on a flat wall derived by Jenkins,<sup>24</sup>

$$N = (1/2) \rho^* g_{12}(0) (1 + e) T, \quad (38)$$

where  $\rho^* = (\rho^p \nu^*)$  is the bulk density of the grain assembly.

Implicit in the formulation of (15) or (37) is the assumption that the spatial and velocity distribution functions remain uncorrelated. We test this assumption by comparing our measurement of the relative normal stress  $\eta = N / \rho^p (1 + e) \leq C_y^- C_y^- \geq$  with the center-averaged volume fraction  $\leq \nu \geq_{\sigma/2}$  of spheres touching the wall; if (37) is correct, then  $\eta = \leq \nu \geq_{\sigma/2}$ . As Fig. 28 shows, the two quantities agree well at intermediate volume fractions and for flows of sufficient width. However, significant disagreements occur at low or high volume fractions, in narrow domains, and in the presence of inelastic spheres. If the flow is rarefied near the wall, the velocity distribution there may be affected by the distribution of particles farther in the interior. Conversely, at high volume fractions the flow near the wall may undergo a phase transition to an ordered solid. Near such a transition one would expect a radical change in the behavior of the collision integral. Similarly, if the Couette cell is too narrow (e.g.,  $L_y/\sigma \approx 5$ ), the spatial distribution at the flat wall is affected by the presence of the thermostat. Finally, our results

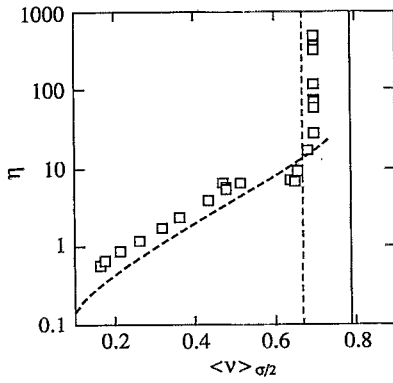


FIG. 29. Relative normal stress  $\eta$  versus  $\langle v \rangle_{\sigma/2}$  for the conditions  $e=0.9$ ,  $\mu=\infty$ ,  $\beta_0=0$ ,  $L_y/\sigma=22.3$ , and  $L_x/\sigma=L_z/\sigma=5.9$ . The squares are the simulation results. The oblique dashed line is the prediction of  $\leq v \geq_{\sigma/2}$  derived from (35) with the assumption  $v^* \approx \langle v \rangle_{\sigma/2}$ . The vertical dashed and solid lines represent  $\langle v \rangle_{\sigma/2} = 0.665$  and  $\pi/4$ , respectively.

indicate that the behavior of  $\eta$  vs  $\leq v \geq_{\sigma/2}$  is nearly independent of friction and tangential restitution. However, as Fig. 28 shows, it depends on the coefficient of normal restitution. The effect of the latter suggests that, like in the simple shear flows of spheres,<sup>30</sup> the grain assembly near the wall experiences significant structural changes with decreasing elasticity. In cases where  $\eta$  differs from  $\leq v \geq_{\sigma/2}$ , one cannot predict the absolute magnitude of the normal stress using (37). Nevertheless, because the spatial distribution contributes equally to each component of the stress, the ratio  $S/N$  is still correctly predicted by Jenkins' theory.

In the interior, as the effects of the walls diminish, the oscillations of the average flow parameters progressively disappear and the local values of the center- and mass-averaged volume fractions become equal to  $v^*$ . Unfortunately, because our simulations fail to produce a constant  $v^*$  across the cell, it is difficult to distinguish the value of this quantity at the wall among the oscillations of the average statistics. However, our experience is that the mass-averaged quantity  $\langle v \rangle_{\sigma/2}$  is a reasonable extrapolation of  $v^*$  at the wall [Fig. 26(a)]. In this context, a plot of  $\eta \approx \leq v \geq_{\sigma/2}$  vs  $\langle v \rangle_{\sigma/2} \approx v^*$  provides a convenient, if approximate, test of the theoretical prediction of  $\leq v \geq_{\sigma/2} = v^* g_{12}(0)$  derived from (35). As Fig. 29 indicates, (35) captures the general trends of the data unless  $\langle v \rangle_{\sigma/2}$  is large. However, it typically underpredicts the magnitude of  $\leq v \geq_{\sigma/2}$  at the wall. Waisman, Henderson, and Lebowitz made a similar observation in their comparisons of the HAB theory for  $g_{12}(0)$  with Monte-Carlo simulations of the spatial distribution function.<sup>37</sup>

At the wall we observe a similar behavior of the relative normal stress  $\eta$  and the dimensionless collision flux (Fig. 30). For an isotropic, homogeneous, unbounded, steady flow of elastic spheres with Maxwellian velocity distribution function, the collisional flux  $\Xi$  of particles striking a plane of normal  $\mathbf{n}$  is

$$\Xi \sigma^3 / \sqrt{T} = -(3\sqrt{2}/\pi^{3/2}) v^* g_{12}(0) \mathbf{n}. \quad (39)$$

Despite the significant departures of the velocity distribution function from the Maxwellian, this expression produces a

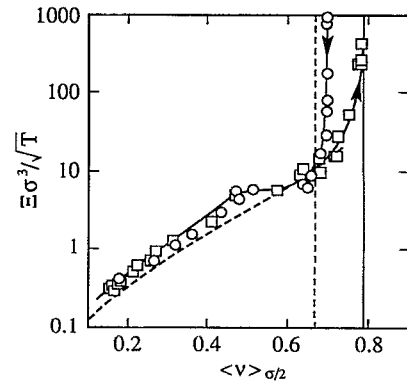


FIG. 30. Normalized collision flux with the wall  $\Xi \sigma^3 / \sqrt{T}$  versus  $\langle v \rangle_{\sigma/2}$  for the conditions  $e=0.9$ ,  $\mu=\infty$ ,  $\beta_0=0$ ,  $L_x/\sigma=L_z/\sigma=5.9$ , and  $L_y/\sigma=22.3$ . The circles and squares represent two independent series of simulations. The arrows indicate the direction of increasing  $U/\sqrt{T_0}$ . The solid lines are visual fits through the data. The oblique dashed line is Eq. (39) assuming  $v^* \approx \langle v \rangle_{\sigma/2}$ . Vertical lines, see Fig. 29. The condensation of the spheres into a two-dimensional crystal at  $\langle v \rangle_{\sigma/2} = \pi/4$  may be an artifact of the simulations with  $L_x=L_z$ .

reasonable estimate of the collision flux at the wall for moderate particle concentrations, if  $\langle v \rangle_{\sigma/2}$  is used as an estimate of  $v^*$  there (Fig. 30). However, for denser grain assemblies, which correspond to low values of  $U/\sqrt{T_0}$  in the simulations, the normal stress and the collision flux increase dramatically (Figs. 29 and 30). Our suggestion is that a phase transition is taking place at the wall. We discuss this behavior next.

## E. Phase transition

If the global shearing  $U/\sqrt{T_0}$  applied to the Couette domain is decreased, the agitated spheres progressively condense near the bottom wall and the collision flux grows asymptotically as  $\langle v \rangle_{\sigma/2}$  approaches a constant value. In this case, the packing is dense enough for the spheres to adopt relative positions that oscillate around a stable arrangement. In this persistent configuration, any further reduction in  $U/\sqrt{T_0}$  raises the collision flux, but it has no effect on the packing fraction.

Generally, this asymptotic packing fraction is not unique. For example, successive simulations that increase  $U/\sqrt{T_0}$  until  $\langle v \rangle_{\sigma/2} \leq 0.65$ , then decrease it again, can produce significantly different asymptotic packings (Fig. 30). This hysteresis in the behavior of the normal stress and the collision flux suggests that once they condense into a critical configuration, the spheres cannot rearrange at a higher packing fraction unless the mean shearing is increased first.

Although the largest theoretical value of  $\langle v \rangle_{\sigma/2}$  would correspond to spheres laid on the wall in a two-dimensional hexagonal close packing ( $\langle v \rangle_{\sigma/2} = \pi\sqrt{3}/6$ ), we have not observed any value of  $\langle v \rangle_{\sigma/2}$  greater than that of the two-dimensional square packing ( $\langle v \rangle_{\sigma/2} \leq \pi/4$ ), even in simulations with  $L_x/L_z \neq 1$ . Perhaps this is because a value of  $\langle v \rangle_{\sigma/2}$  greater than  $\pi/4$  at the wall would correspond to a packing in the bulk that may not be sheared without dilation. Because such dense, agitated packings are associated with high collision frequencies, their behavior in a real system may be more

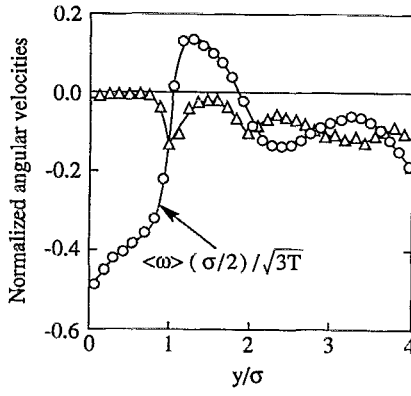


FIG. 31. Normalized profiles of mass-averaged angular velocities for the conditions of Fig. 22. The circles and triangles represent the  $z$  component of  $\langle \omega \rangle (\sigma/2)/\sqrt{3T}$  and  $(1/2)\nabla \times \langle c \rangle (\sigma/2)/\sqrt{3T}$ , respectively. The solid lines are visual fits through the data. Similar, albeit noisier, profiles are obtained through center averaging.

complex than that predicted by the present simulations. For example, one may expect significant changes in the collision properties of real spheres if the average time between collisions becomes smaller than a characteristic time for the propagation of waves within the particle.

The profiles of the volume fraction and the first and second moments of velocities (Figs. 25, 26, and 31) clearly suggest that the wall constraints the spheres to arrange in layers. Under conditions that promote condensation of the spheres near the flat boundary (e.g., low values of  $U/\sqrt{T_0}$ , or inelasticity), the layer adjacent to the wall appears to behave as a two-dimensional array. The changes in the behavior of the collision integral that accompany the condensation thus resemble a two-dimensional phase transition from a dense gas to an ordered solid.

In this context, Jenkins and Shahinpoor<sup>38</sup> review the theory and Kawamura,<sup>39</sup> who successfully predicts a first-order phase transition between solid and fluid states of identical disks. Kawamura estimates a configurational entropy for a system of disks in terms of the probability for each of the possible arrangements that the disks may exhibit. He further considers a vibrational entropy associated with the thermal fluctuations of the disk centers about their mean position. Adopting a free energy that incorporates the total entropy, a first-order phase transition occurs if this free energy may be minimized in both an ordered and disordered state having the same free energy. Jenkins and Shahinpoor show that such a transition occurs as

$$N_{\Delta}/\rho_{\Delta}T_{\Delta}=6.9, \quad (40)$$

where  $N_{\Delta}$  and  $T_{\Delta}$  are the pressure and temperature of the two-dimensional assembly, respectively, and  $\rho_{\Delta}$  is the two-dimensional bulk density of an hexagonal close packing of surface fraction  $\nu_{\Delta}=\pi\sqrt{3}/6$ . For an isotropic, homogeneous, unbounded, steady flow of elastic disks, the pressure is

$$N_{\Delta}=\rho^p\nu_{\Delta}^*[1+2\nu_{\Delta}^*g_{\Delta}(0)]T_{\Delta}, \quad (41)$$

where  $g_{\Delta}(0)$  is the spatial distribution function of two identical disks at contact,

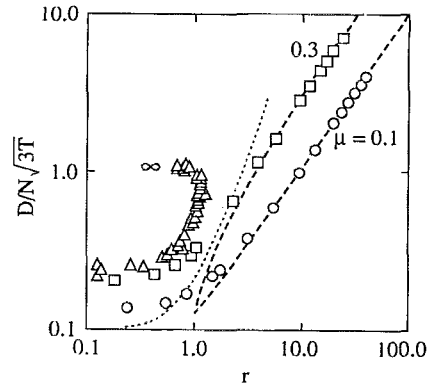


FIG. 32. Normalized dissipation of fluctuation energy for the conditions  $e=0.9$ ,  $\beta_0=0$ , and  $L_x/\sigma=L_y/\sigma=5.9$ . The circles and squares are  $L_y/\sigma=5.9$ , and  $\mu=0.1$  and  $0.3$ , respectively. The dashed lines are the corresponding predictions of Jenkins in the small friction/all sliding limit. The triangles are  $\mu=\infty$  and  $L_y/\sigma=5.9$  or  $22.3$ . The dotted line is Jenkins' prediction in the large friction/no sliding limit.

$$g_{\Delta}(0)=(16-7\nu_{\Delta}^*)/16(1-\nu_{\Delta}^*)^2 \quad (42)$$

and  $\nu_{\Delta}^*$  is the bulk surface fraction of the disks.<sup>40,41</sup> Jenkins<sup>42</sup> combines (40) through (42) to produce an estimate of the surface fraction  $\nu_{\Delta}^* \approx 0.665$  in excellent agreement with the value of  $\langle \nu \rangle_{\sigma/2}$  where we observe the two-dimensional phase transition (Figs. 29 and 30).

## F. Dissipation

An important intermediate in Jenkins' theory is the calculation of the average dissipation of fluctuation energy. In the small friction/all sliding limit, he obtains

$$\frac{D}{N\sqrt{3T}}=\mu\left(r-\frac{21}{16}(1+e)\mu+\frac{1}{10r}\right)+\frac{3}{8}(1-e)+o\left(\frac{1}{r^3}\right). \quad (43)$$

and in the large friction/no sliding limit,

$$\frac{D}{N\sqrt{3T}}=\frac{3}{28}\left(\frac{1-\beta_0^2}{1+e}\right)(2r^2+1)+\frac{3}{8}(1-e). \quad (44)$$

For low values of friction, the predictions of (43) are excellent when  $r$  is large (Fig. 32). Thus in the small friction/all sliding limit, Jenkins calculates the correct form of both the dynamic friction,  $S \sim \mu N$ , and the dissipation,  $D/N\sqrt{3T} \sim \mu r$ , as  $r \rightarrow \infty$ . Unfortunately, because at high slip the flux is a difference between two large numbers that grow linearly with  $r$ , the accuracy of these predictions do not necessarily yield the correct flux of fluctuation energy in that limit: from (17),

$$Q=-\mathbf{g}_0 \cdot \mathbf{M}-D=g_0S-D. \quad (45)$$

Thus, in Jenkins' formulation,



$$\frac{Q}{N\sqrt{3T}} \sim r\mu - \frac{D}{N\sqrt{3T}}$$

$$= r\mu - r\mu + \frac{3}{8} \left( \frac{7}{2} (1+e)\mu^2 - (1-e) \right), \quad (46)$$

so the normalized flux is constant at large  $r$ , see (23). It is this constant difference that the theory has yet to capture exactly.

### G. Spin

In the absence of a reliable flow theory for frictional spheres, Jenkins ignores the spin fluctuations of the particles, so the instantaneous slip at the contact point only differs from the mean through fluctuations of the velocity of the center of mass,

$$\mathbf{g} = \mathbf{g}_0 + \mathbf{C}. \quad (47)$$

Consequently, because the impulse and the change in kinetic energy are only functions of  $\mathbf{g}$ ,  $\mathbf{n}$ ,  $m$ ,  $e$ ,  $\mu$ , and  $\beta_0$ , their integrations over the velocity distribution function produce expressions for  $S/N$  and  $Q/N\sqrt{3T}$  that depend only upon  $\mathbf{g}_0$ ,  $T$  and the collision properties. Therefore, the theory predicts the dynamic friction coefficient and the normalized flux in terms of the normalized mean slip at the point of contact. In practical situations, it remains to calculate the slip from the mean velocity of the center of mass and the mean angular velocity of the particles. Unfortunately, without a flow theory for frictional spheres, the mean angular velocity is not predictable.

In order to produce boundary conditions that can be applied to existing theories for spheres, Jenkins suggests that, as a first approximation, the mean angular velocity of the spheres equals the angular velocity of the mean flow,

$$\langle\langle\boldsymbol{\omega}\rangle\rangle = (1/2)\nabla \times \langle\langle\mathbf{c}\rangle\rangle. \quad (48)$$

This is the relation between these quantities in a steady, simple shear with uniform velocity gradient.<sup>43</sup> Unfortunately, as Fig. 31 indicates, the two angular velocities are considerably different near the wall, so (48) is not a reliable estimate of  $\langle\langle\boldsymbol{\omega}\rangle\rangle$  there. However, they converge in the interior, where the influence of the wall diminishes. Generally, the anomalous values of these quantities appear to be located primarily within the first two layer of particles ( $0 \leq y/\sigma \leq 2$ ). In the first layer, particles spin in a direction consistent with their relative slip with the wall ( $\omega_z < 0$ ). In the second, they spin in the opposite direction, so the mean value  $\langle\langle\boldsymbol{\omega}\rangle\rangle$  nearly vanishes at  $y = \sigma$ .

Finally, Fig. 33 reveals considerable variations of the spin with the width of the Couette cell and the frictional properties of interior particles. Thus our simulations suggest that a theory for the spin should incorporate details of the flow in the interior.

### V. CONCLUSIONS

In this paper, we have tested the predictions of Jenkins for the interaction of a rapid granular flow of spheres and a flat, frictional wall. We find that the dynamic friction coefficient

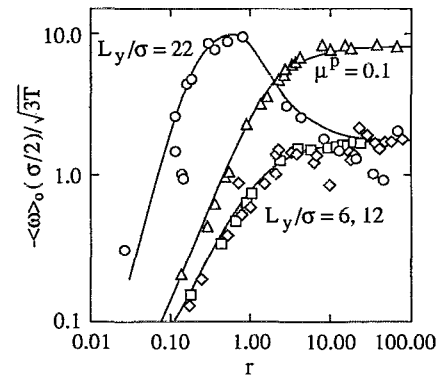


FIG. 33. Normalized magnitude of the mean spin at the wall in the  $z$  direction for the conditions  $e=0.9$ ,  $\mu=0.3$ ,  $\beta_0=0$ , and  $L_x/\sigma=L_z/\sigma=5.9$ . The squares, diamonds, and circles are  $L_y/\sigma=5.9$ , 11.7, and 22.3, respectively. The triangles are  $\mu^p=0.1$ . The solid lines are visual fits through the data.

and the normalized flux of fluctuation energy depend primarily on the collision properties of the boundary and the normalized mean slip of the contact point. For relatively low friction, the theory correctly predicts the trends observed in the simulations. In particular, we confirm that the ratio of the shear and normal stresses is always smaller than the friction coefficient of individual spheres. For very large friction, our simulations show that, as the mean shear increases, the particles tend toward a limit where they roll without slipping. Conversely, for small values of the mean shear, we suggest that the assembly of spheres at the wall undergoes a two-dimensional phase transition from a dense gas to an ordered solid. Finally, our examination of Jenkins' assumptions indicates where his theory may be improved. Notably, we suggest that a new theory should predict the mean spin of the particles at the boundary, so the slip at the contact point may be evaluated in terms of the conditions in the interior.

### ACKNOWLEDGMENTS

The author is indebted to Mark A. Hopkins, who provided the collision and search algorithms that simulate three-dimensional rapid flows of spheres, and to James T. Jenkins, who offered his support and encouragement through countless valuable discussions. This work was supported by the Pittsburgh Energy Technology Center of the U.S. Department of Energy under the Granular Flow Advanced Research Objective through Contract No. DE-AC22-91PC90183.

<sup>1</sup>S. B. Savage and M. Sayed, "Stresses developed by dry cohesionless granular materials sheared in an annular shear cell," *J. Fluid Mech.* **142**, 391 (1984).

<sup>2</sup>D. M. Hanes and D. L. Inman, "Observations of rapidly flowing granular-fluid materials," *J. Fluid Mech.* **150**, 357 (1985).

<sup>3</sup>K. C. Craig, R. H. Buckholz, and G. Domoto, "The effects of shear surface boundaries on normal and shear stresses for rapid shearing flow of dry cohesionless metal powder—An experimental study," *J. Tribol.* **109**, 232 (1987).

<sup>4</sup>C. S. Campbell and A. Gong, "Boundary conditions for two-dimensional granular flows," in *Proceedings of the Sino-US Symposium on Multiphase Flows* (Zhejiang University Press, Hangzhou, 1987), pp. 278–283.

<sup>5</sup>M. Y. Louge, J. T. Jenkins, and M. A. Hopkins, "Computer simulations of rapid granular shear flows between parallel bumpy boundaries," *Phys. Fluids A* **2**, 1042 (1990).

- <sup>6</sup>H. Kim and A. D. Rosato, "Particle simulations of the flow of smooth spheres between bumpy boundaries," *Advances in Micromechanics of Granular Materials*, edited by H. H. Shen, M. Satake, M. Mehrabadi, C. S. Chang, and C. S. Campbell (Elsevier, New York, 1992), pp. 91–100.
- <sup>7</sup>J. T. Jenkins and M. W. Richman, "Boundary conditions for plane flows of smooth, nearly elastic, circular disks," *J. Fluid Mech.* **171**, 53 (1986).
- <sup>8</sup>J. T. Jenkins, "Rapid flows of granular materials," in *Non-Classical Continuum Mechanics*, edited by R. J. Knops and A. A. Lacey (Cambridge University Press, Cambridge, 1987), pp. 213–225.
- <sup>9</sup>M. W. Richman, "Boundary conditions based upon a modified Maxwellian velocity distribution function for flows of identical, smooth, nearly elastic spheres," *Acta Mech.* **75**, 227 (1988).
- <sup>10</sup>D. M. Hanes, J. T. Jenkins, and M. W. Richman, "The thickness of steady plane shear flows of circular disks driven by identical boundaries," *J. Appl. Mech.* **55**, 969 (1988).
- <sup>11</sup>G. C. Pasquarell and N. L. Ackermann, "Boundary conditions for planar granular flows," *ASCE J. Eng. Mech.* **115**, 1283 (1989).
- <sup>12</sup>G. C. Pasquarell, "Granular flows: Boundary conditions for slightly bumpy walls," *ASCE J. Eng. Mech.* **117**, 312 (1991).
- <sup>13</sup>D. A. Augenstein and R. Hogg, "An experimental study of the flow of dry powders over inclined surfaces," *Powder Tech.* **19**, 205 (1978).
- <sup>14</sup>T. G. Drake and R. L. Shreve, "High speed motion pictures of nearly steady, uniform, two-dimensional, inertial flows of granular materials," *J. Rheol.* **30**, 981 (1986).
- <sup>15</sup>M. Ishida and T. Shirai, "Velocity distributions in the flow of solid particles in an inclined open channel," *J. Chem. Eng. Jpn.* **12**, 46 (1979).
- <sup>16</sup>S. B. Savage, "Gravity flow of cohesionless granular materials in chutes and channels," *J. Fluid Mech.* **92**, 53 (1979).
- <sup>17</sup>H. Ahn, C. E. Brennen, and R. H. Sabersky, "Measurements of velocity, velocity fluctuation, density, and stresses in chute flows of granular materials," *J. Appl. Mech.* **58**, 792 (1991).
- <sup>18</sup>C. S. Campbell and C. E. Brennen, "Computer simulations of granular shear flows," *J. Fluid Mech.* **151**, 167 (1985).
- <sup>19</sup>C. S. Campbell and C. E. Brennen, "Chute flows of granular materials: Some computer simulations," *J. Appl. Mech.* **52**, 172 (1985).
- <sup>20</sup>Y. Zhang and C. S. Campbell, "The interface between fluid-like and solid-like behavior in two-dimensional granular flows," *J. Fluid Mech.* **237**, 541 (1992).
- <sup>21</sup>M. Nakagawa and T. Imaizumi, "Simulations of rapid bimodal granular flows," in *Advances in Micromechanics of Granular Materials*, edited by H. H. Shen, M. Satake, M. Mehrabadi, C. S. Chang, and C. S. Campbell, (Elsevier, New York, 1992), pp. 131–140.
- <sup>22</sup>O. R. Walton, "Numerical simulations of inclined chute flows of mono-disperse, inelastic, frictional spheres," *Mech. Mater.* **16**, 239 (1993).
- <sup>23</sup>P. C. Johnson and R. Jackson, "Frictional-collisional constitutive relations for granular materials with applications to plane shearing," *J. Fluid Mech.* **176**, 67 (1987).
- <sup>24</sup>J. T. Jenkins, "Boundary conditions for rapid granular flows: Flat, frictional walls," *J. Appl. Mech.* **59**, 120 (1992).
- <sup>25</sup>M. A. Hopkins and M. Y. Louge, "Inelastic microstructure in rapid granular flows of smooth disks," *Phys. Fluids A* **3**, 47 (1991).
- <sup>26</sup>N. Maw, J. R. Barber, and J. N. Fawcett, "The oblique impact of elastic spheres," *Wear* **38**, 101 (1976).
- <sup>27</sup>N. Maw, J. R. Barber, and J. N. Fawcett, "The role of elastic tangential compliance in oblique impact," *J. Lubr. Technol.* **103**, 74 (1981).
- <sup>28</sup>O. R. Walton, "Granular solids flow project," Quarterly Report No. UCID-20297-88-1, Lawrence Livermore National Laboratory, January–March 1988.
- <sup>29</sup>S. Foerster and M. Y. Louge, "Measurements of the collision properties of small spheres," *Phys. Fluids* **6**, 1108 (1994).
- <sup>30</sup>M. A. Hopkins, J. T. Jenkins, and M. Y. Louge, "On the structure of 3D shear flows," *Mech. Mater.* **16**, 179 (1993).
- <sup>31</sup>O. R. Walton and R. L. Braun, "Viscosity and temperature calculations for assemblies of inelastic frictional disks," *J. Rheol.* **30**, 949 (1986).
- <sup>32</sup>J. T. Jenkins and M. W. Richman, "Plane simple shear of smooth, inelastic, circular disks: The anisotropy of the second moment in the dilute and dense limits," *J. Fluid Mech.* **192**, 313 (1988).
- <sup>33</sup>T. G. Drake, "Granular flow, physical experiments and their implications for microstructural theories," *J. Fluid Mech.* **225**, 12 (1991).
- <sup>34</sup>D. Henderson, F. F. Abraham, and J. A. Barker, "The Ornstein–Zernike equation for a fluid in contact with a surface," *Mol. Phys.* **31**, 1291 (1976).
- <sup>35</sup>M. S. Wertheim, "Exact solution of the Percus–Yevick integral equation for hard spheres," *Phys. Rev. Lett.* **10**, 321 (1963).
- <sup>36</sup>W. R. Smith and D. Henderson, "Analytical representation of the Percus–Yevick hard-sphere radial distribution function," *Mol. Phys.* **19**, 411 (1970).
- <sup>37</sup>E. Waisman, D. Henderson, and J. L. Lebowitz, "Solution of the mean spherical approximation for the density profile of a hard-sphere fluid near a wall," *Mol. Phys.* **32**, 1373 (1976).
- <sup>38</sup>J. T. Jenkins and M. Shahinpoor, "Macroscopic phase transition in two-dimensional granular materials," in *Mechanics of Granular Material*, edited by J. T. Jenkins and M. Satake (Elsevier, New York, 1983), pp. 339–346.
- <sup>39</sup>H. Kawamura, "A simple theory of hard disk transition," *Prog. Theor. Phys.* **61**, 1584 (1979).
- <sup>40</sup>L. Verlet and D. Levesque, "Integral equations for classical fluids III. The hard discs system," *Mol. Phys.* **46**, 969 (1982).
- <sup>41</sup>J. T. Jenkins, "Balance laws and constitutive relations for rapid flows of granular materials," in *Constitutive Models of Deformation*, edited by J. Chandra and R. P. Srivastav (SIAM, Philadelphia, 1987), pp. 109–119.
- <sup>42</sup>J. T. Jenkins (private communication, 1993).
- <sup>43</sup>C. S. Campbell, "The stress tensor for simple shear flows of a granular material," *J. Fluid Mech.* **203**, 449 (1989).